Report on the Maidanak site testing campaign in July 1998 (Maidanak-98)

A. Tokovinin, V. Kornilov, R. Conan, A. Ziad, F. Martin, S. Ilyasov, S. Ehgamberdiev, Y. Tillaev, K. Sultanov, M. Sarazin

November 30, 1998

Abstract

Various parameters of the atmospheric turbulence above the Maidanak observatory located in Uzbekistan Republik were measured on 9 nights in July 1998 with three complementary instruments: Differential Image Motion Monitor (DIMM), Generalized Seeing Monitor (GSM) and two Scintillation Photometers (SP). Median FWHM seeing was equal to $0.64''$, the median wavefront outer scale $\mathcal{L}_0 = 25.9$ m, median isoplanatic angle $\theta_0 = 2.48''$. Temporal evolution of the wavefront can be described by several layers moving at slow velocities (mostly less than 2 m/s and never exceeding 10 m/s) with predominant direction from the West. There was no correlation between wavefront velocity and the wind velocity at ground level. Turbulence in the $3-30$ m surface layer was not important, contributing on the average 10% to the total C_n^2 integral (except on one occasion when it was very strong and dominant). Independent measurements of the free-atmosphere seeing (excluding the first kilometer above ground) obtained by a new scintillation-based technique suggest that it was typically $0.3''-0.4''$, and hence the overall seeing was usually dominated by the boundary layer.

This mission has demonstrated the potential of modern optical techniques for complete turbulence characterization. Good seeing, large isoplanatic angle and slow wind indicate that Maidanak is a promising site for high-angular-resolution observations by interferometry and adaptive optics.

Contents

1 Introduction

This site testing campaign was organized in the framework of the project INTAS 96-0367 "Characterization of Maidanak Observatory among the Major International Ground Based Astronomical Facilities of the Future" (project leader Marc Sarazin, ESO). Four institutions participate in this project (team leaders are also named):

1. *European Southern Observatory (ESO)*, Garching, Germany - M. Sarazin
2. *Ulugh Beg Astronomical Institute of the Uzbek Academy of Sciences (UBAI)*, Tashkent, Uzbekistan Republik - S. Ilyasov
3. *Université de Nice (UN)*, Nice, France - F. Martin
4. *Sternberg Astronomical Institute (SAI)*, Moscow, Russia - V. Kornilov.

The aim of this mission was to make the measurements of the atmospheric parameters relevant to astronomical observations at the potentially very good site - Mt. Maidanak in Uzbekistan. A seeing statistics at Maidanak over the period of more than 1 year have been collected by the team of UBAI (Ilyasov et al., 1998) and shows it to be among the best sites known to date. They used the Differential Image Motion Monitor (DIMM) provided by ESO. During this mission the seeing was measured also by the Generalized Seeing Monitor (GSM) developed at the UN. Below we give the comparison of these independent data sets which validates the much larger DIMM database and confirms the excellent quality of Maidanak seeing. The GSM instrument also measures other atmospheric parameters which are of particular importance to the high angular resolution astronomical techniques like adaptive optics and interferometry. These parameters are the wavefront outer scale $\mathcal{L}_0$, the wavefront coherence time τ_0 and the isoplanatic angle θ_0 . These data are obtained at Maidanak for the first time. Finally, the SAI team furnished complementary data on stellar scintillation and isoplanatic angle which give better understanding of the high-altitude turbulence over Maidanak.

The three teams participated in this campaign. Their composition and responsibility are listed below:

1. Tashkent team (Ilyasov Sabit, Ehgamberdiev Shukrat, Tillaev Yusuf, Sultanov Khatam, Sadibekova Tatyana): DIMM operation and data reduction, logistic support on the site (transport, infrastructure preparation, etc).
2. Nice team (Martin François, Ziad Aziz, Conan Rodolphe, Borgnino Julien): GSM operation and data reduction.
3. Moscow team (Kornilov Victor, Tokovinin Andrei): scintillation measurements, GSM operation.

2 Instrument description

2.1 Differential seeing monitor (DIMM)

The DIMM instrument was developed at ESO by M.Sarazin. It is a simplified and portable version of the standard ESO DIMM described by Sarazin & Roddier (1990), called DIMM5. The instrument parameters are:

- Telescope Celestron 11 (D=276 mm, F=2800 cm)

- Pupil mask: aperture diameter 5 cm, baseline 20 cm. One aperture has a prism (angle 195$''$, n=1.4) to separate the images in the focal plane. Baseline is oriented in the declination direction.

- CCD camera ST5, equipped with the TC255 CCD (10 micron square pixels, 320 by 240). The camera permits fast image acquisition in the half-frame transfer mode, with minimum exposure time of 10 ms.

- PC AT computer with a DIMM software originally written by P. Wood (MSSO) for ST4 camera and ported to ST5 at ESO.

Standard DIMM operation consists in pointing a bright star near zenith and taking continuous exposures controlled by the software (approximately every 2.5 seconds). Image centroids are computed for each frame. Seeing is estimated from the rms differential image motion in the direction of the baseline (longitudinal) and perpendicular to the baseline (transverse).

In order to compensate for the finite duration of exposure time, a method of interlaced exposures is used (Sarazin, 1998): exposures of 10 and 20 ms are taken sequentially. So, every 4 minutes two seeing estimates (average of longitudinal and transverse) corresponding to 10 and 20 ms exposures are obtained. The final value of seeing is calculated by linear extrapolation to zero exposure time. During our mission this correction was usually small (the differential AA variance is increased by 1.1-1.4 times) because wind speed was low.

During the mission, a small error in the DIMM software was found, which resulted in the calculated seeing being too low by a constant factor. To correct for this, the seeing angles measured by DIMM 5 must be multiplied by $1.12 = (0.55/0.5)^{6/5}$. This correction was systematically applied to all DIMM data discussed below.

2.2 Generalized Seeing Monitor (GSM)

GSM was developed at Nice University in collaboration with SAI. Its early version is described in (Martin et al, 1994; Agabi et al. 1995). The full 4-channel version was first extensively used in 1997 during the La Silla campaign in Chile (Martin et al. 1998; Tokovinin et al. 1998). GSM consists of 4 identical units for angle of arrival measurements, with associated electronics for data acquisition and a PC computer. Each unit has a 10 cm Maksutov telescope and a detection module to measure the stellar image position using a grating in the focal plane together with fast (200 Hz) modulation. Ligh transmitted by the grating is detected by the PMT in pulse counting mode. All 4 units work synchronously and provide the angle of arrival (AA) data with 5 ms temporal resolution.

The units were equipped with the simple but rigid alt-azimuth supports to point them to the Polar star. Field of view of $13.7'$ permits observations during 30 min without repointing. Units 1 and 2 had a common support for seeing measurement in differential mode (baseline 25 cm), like DIMM. GSM was installed on a 3 meter high concrete pier built especially for this mission (Fig. 1). Objectives were 3.4 m above ground level. Unit 3 was located on the same pier to the east (0.8 m from the center of the differential unit), and unit 4 was located 1.5 m below (1.9 m above ground). All units measure AA fluctuations in the horizontal direction. Thus the baselines formed by units 1-2, 1-3, 2-3 are longitudinal, baselines 1-4 and 2-4 are approximately transverse, and baseline 3-4 is oblique. Such geometrical arrangement was chosen to explore the 2D structure of the wavefront and to determine its effective speed. Baseline lengths are optimized for maximum sensitivity to the outer scale effects for the expected decametric outer scale values. In the previous GSM missions (La Silla, Chili; Oukaimeden, Marocco; El Pachon, Chili) all GSM units were located in a horizontal plane, but, when projected onto the wavefront, our present "3D"arrangement results in the same configuration.

Data acquisition was typically 2 minutes long, repeated every 4 minutes. Data were processed immediately after acquisition. Processing includes calculation of the AA variance in

Figure 1: GSM and its support structure at Maidanak. Concrete piers have cross-section of 40x40 cm, the height of the structure above ground is 3.0 m. Units 1, 2, 3 are located at top, while unit 4 is 1.5 m below, in order to probe the surface layer turbulence.

each unit and AA covariances which, after suitable normalisation, were compared to the pre-calculated table to find the wavefront outer scale $\mathcal{L}_0$. The six values of $\mathcal{L}_0$, corresponding to the 6 baselines of GSM, are found, and their median is taken as final result.

Seeing is calculated from the differential AA variance in units 1 and 2, like in DIMM. Small corrections for photon and scintillation noise are made. Correction for finite exposure time is also performed by calculating the AA variance with 5 ms and 10 ms temporal resolution and extrapolating to the 0 ms exposure time. This latter correction was typically about 10%, because seeing at Maidanak is rather slow. Additional estimation of seeing comes from the AA variance in each unit, with non-negligible correction for finite outer scale. A good match between differential and absolute seeing estimates is a sign that the support vibration was not important, which is a necessary condition for correct GSM operation. Also, the difference between AA variance measured by the units 3 and 4 was used to estimate the importance of ground layer turbulence, because these units were installed at different heights above ground (3.4 and 1.9 m, respectively).

The isoplanatic angle was calculated from the scintillation index, as prescribed by Loos & Hogge (1987). Our time resolution of 5 ms is not sufficient for unbiased measurement of scintillation, but we corrected for time averaging in the same manner as for the AA.

Wavefront speed measurements from the cross-correlations of the AA fluctuations at all baselines will be described in Ch. 4.1.

2.3 Scintillation measurements with the 4-channel photometer

These measurements were conducted at the 60 cm reflector (f=7.5 m) installed in the sliding roof pavillon. We used two scintillation photometers with photon counting PMT light detectors, both with the same data acquisition system and PC computer.

2.3.1 The multi-color scintilation photometer SP1

The aim of the first experiment (called SP1 hereafter) is to measure the power (variance) of scintillations simultaneously in three spectral bands (B, V, R) and quasi-simultaneously

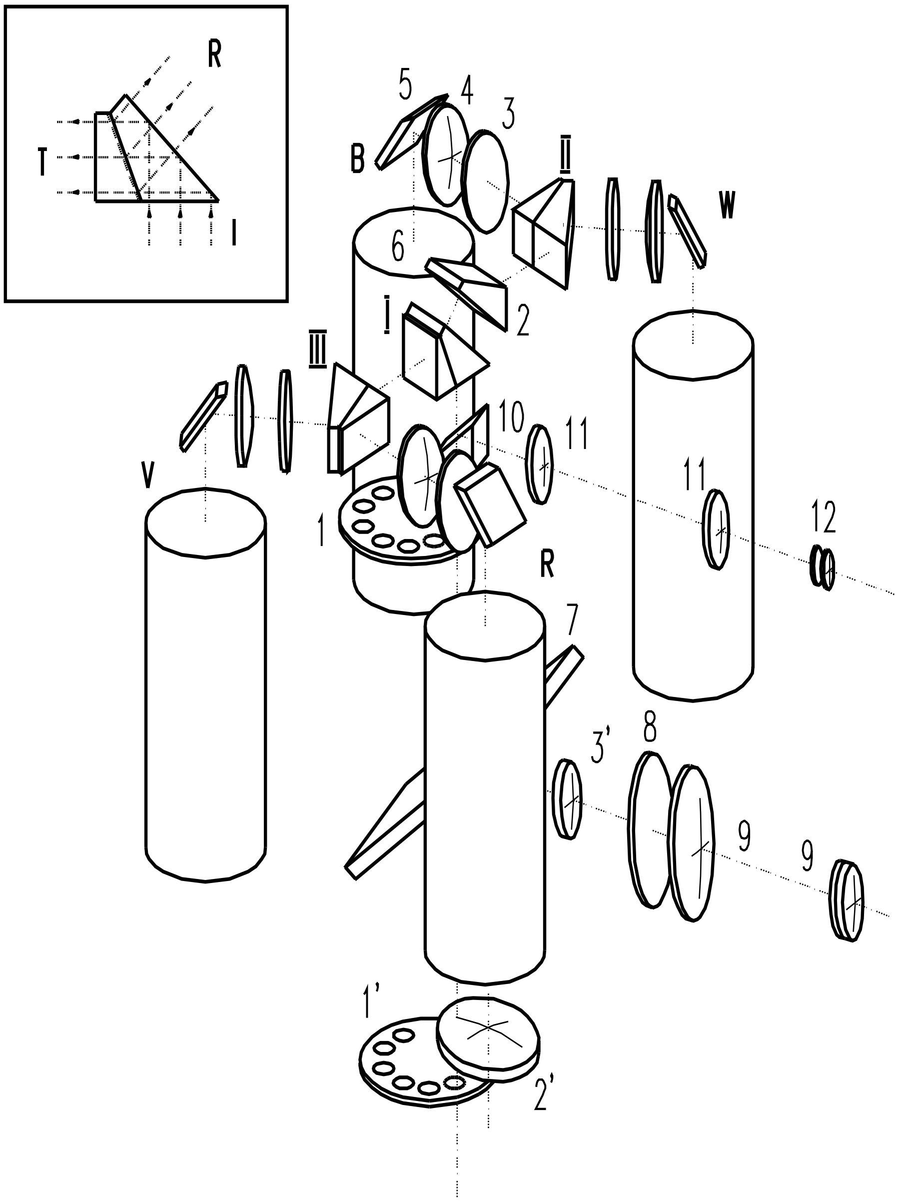

Figure 2: Optical layout of the 4-channel photometer modified for scintillation measurements. Components of the standard photometer are: 1 - disk with apertures (now in pupil plane), I, II, III - dichroic beamsplitters (shown in the insert), 2 - auxilliary prism, 3 - glass filter, 4 - Fabry lens, 5 - plane mirror, 6 - photomultiplier, 7 - mirror of wide field viewer, 8, 9 - optics of wide field viewer, 10 - prism of the aperture viewer, 11, 12 - optics of the aperture viewer. Additional elements installed for the scintillation measurements include the new focal aperture 1' with a 160 mm lens 2' and a lens 3' for wide field viewer adaptation.

in 8 entrance apertures, including the annular "isoplanatic" aperture, as explained in next sub-section. The SP1 is a modified 4-channel WBVR stellar photometer with light splitting by dichroic mirrors (Kornilov & Krylov, 1990; Kornilov 1998). The optical layout of the photometer is given in Fig. 2. The light beam from the telescope arrives from the bottom of the figure. In the telescope focal plane the disk 1 with field apertures is placed, controlled by a stepper motor. The dichroic beamsplitter I separates the "blue" ($\lambda < 500$ nm) and "red" ($\lambda > 500$ nm) light beams. The blue beam passes through the auxiliary prism 2 to the beamsplitter II, which divides the W ($\lambda < 380$ nm) and B ($\lambda > 380$ nm) channels. Similarly, the beamsplitter III directs the light with $\lambda > 610$ nm to the channel R, and shorter wavelengths to the channel V. In each channel the light goes through the color filter 3 and Fabry lens 4, then it is deflected by mirror 5 to the photocathode 6 of the respective PMT. The wide field viewer consists of the switchable mirror 7, plane plate with a cross 8, and the Kellner ocular 9 with f=90 mm. The aperture viewer includes the sliding prism 10, the reimaging symmetric lens 11 and a 20x ocular 12.

For scintillation measurements the additonal units were installed into this photometer. The focal plane was shifted forward (in the direction of the secondary mirror) by 170 mm, and a 2 mm (corresponding to 60 arcseconds field) focal aperture 1' was installed. A lens 2' with f=160 mm placed near the new focal plane was added to form the image of the pupil in the plane of aperture wheel 1, which now plays the role of pupil apertures. This lens was shifted laterally from the main optical axis by approximately 4 mm in order to bring the light from the unvigneted part of the primary mirror segment to the pupil apertures. Additional lens 3' is placed on the optical axis when the wide field mirror 7 is switched on. It forms the magnified image of the focal aperture 1' in the focal plane of the ocular 9, for the purpose of star centering.

The apertures are changed under computer control. The switching time is 0.11 s, with 0.02 s more for vibration attenuation. Characteristics of the apertures used for scintillations measurements are given in the Table below (d - physical diameter, D - diameter projected to the pupil plane). The aperture diameters were determined in the standard photometer configuration by measuring the stellar transit time, with 5% precision for small apertures and 2% precision for large apertures. The flux ratio in different apertures provides an additional control of the correct diameter values.

Number	1	2	3	4	7	8	9	10
d, mm	0.30	0.59	1.01	1.52	1.91	2.29	3.32	2.16 (double)
D, cm	1.35	2.66	4.59	6.91	8.68	10.41	15.08	9.82

2.3.2 The principle of isoplanatic angle measurements

The last aperture has a central obscuration (relative diameter $\epsilon = 0.4$) and a projected diameter of 10 cm. It is thus exactly similar to the GSM apertures. It can be shown that the scintillation index measured with such aperture provides a good estimate of the isoplanatic angle. This idea is due to Loos & Hogge (1979). The scintillation in a small aperture produced by a thin turbulent layer at an altitude h is proportional to $h^{5/6}$, and for a very large aperture the altitude dependence is h^2. So, for some intermediate aperture size (which is in fact close to 10 cm) the altitude dependence must be not very far from $h^{5/3}$. The isoplanatic angle θ_0 as defined by Fried (1982) is proportional to the $C_n^2(h)$ integral over altitude with $h^{5/3}$ weighting.

Let us give here some formulae. The scintillation index s^2 is defined as the normalized variance of received light flux I, $s^2 = \sigma_I^2 / < I >^2$. Its relation to the altitude turbulence profile $C_n^2(h)$ is given by

$$s^2 = \int_0^\infty \mathrm{d}h C_n^2(h) W(h), \tag{1}$$

where the weighting function $W(h)$ is

$$W(h) = 16\pi^2 \cdot 0.033 k^2 \int_0^\infty \mathrm{d}f f^{-8/3} \sin^2[f^2 h/(2k)] A(f). \tag{2}$$

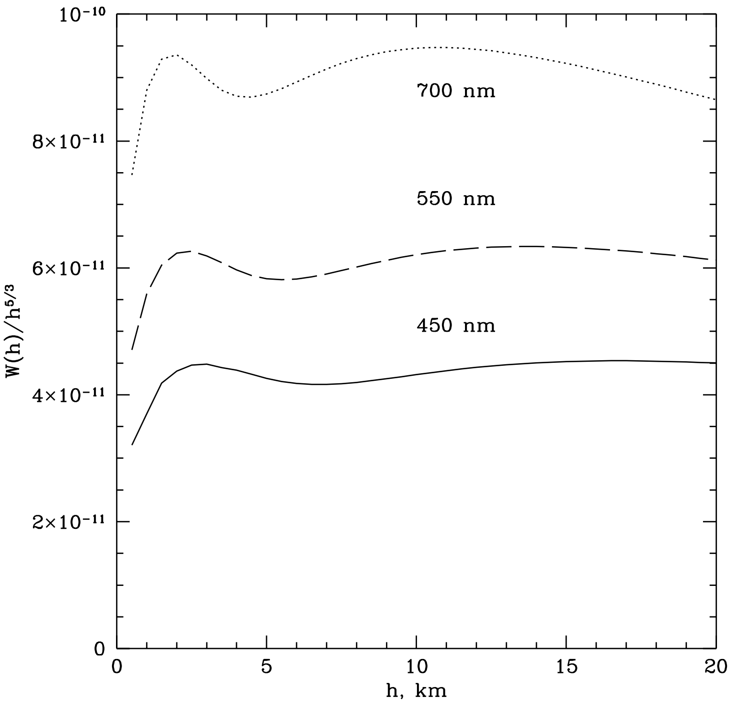

Figure 3: Ratio of the weighting functions corresponding to a 10-cm circular aperture with 0.4 central obscuration to $h^{5/3}$, at three wavelengths: 450 nm (full line), 550 nm (dashed line), and 700 nm (dotted line). Units on vertical axis are m^{-2}.

Here $k = 2\pi/\lambda$, f is the modulus of the spatial frequency.

The function $A(f)$ is a normalized Fourier transform of aperture transmission. In our case, i.e. for an aperture of diameter D with a central obscuration ϵ, it is

$$A(f) = \left[\frac{2J_1(fD/2)}{fD/2} - \epsilon^2 \frac{2J_1(\epsilon fD/2)}{\epsilon fD/2}\right]^2 (1-\epsilon^2)^{-2}. \tag{3}$$

Example of a weighting function calculation for a double-annulus aperture can be found in Krause-Polstorf et al. (1993). The units for weighting function are $m^{-1/3}$. The ratio of the actual weighting functions to $h^{5/3}$ is plotted in Fig. 3 for the 3 colors (B, V, R bands, central wavelengths 450, 550, 700 nm). Isoplanatic angle θ_0 at zenith can be calculated from normalised intensity fluctuations s^2 measured with such aperture at a zenith distance z as

$$\theta_0 = A'(s^2)^{-0.6}(\sec z)^{1.6}. \tag{4}$$

The calibration coefficient A' depends on the wavelength. It also weakly depends on the altitude of a turbulent layer, because the ratio $W(h)/h^{5/3}$ is not exactly constant. We fixed this ratio for $h = 10$ km and calculated the coefficients to obtain the isoplanatic angle at 500 nm wavelength from the scintillation measured in B, V, R bands with our annular aperture (A' = 0.2009, 0.1963, and 0.1893 arcseconds, respectively).

2.3.3 Signal acquisition

The photometer works in the photon counting mode. Fast pulse amplifiers with 200 μV sensitivity and 4 ns response time are used. The pulses are fed by a coaxial cable to the 100 MHz counters which are located on the interface board in the ISA slot of the PC computer. For this experiment the exposure time of 1 ms was used (0.99 ms accumulation with 0.01 ms pause).

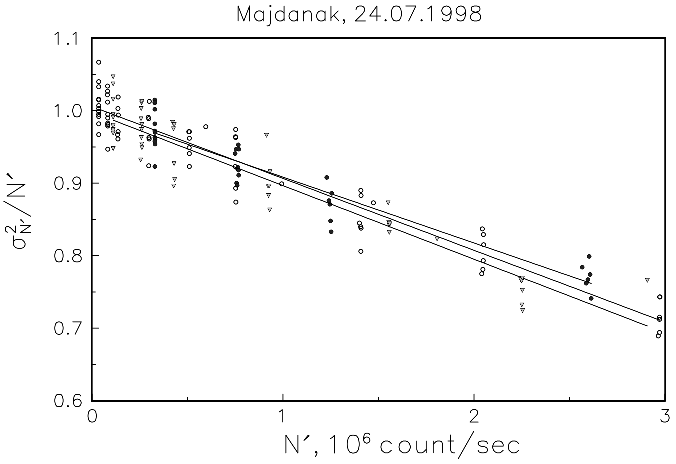

Figure 4: The ratio of signal dispersion $\sigma^2_{N'}$ to the count rate N', in function of the count rate. The linear fits correspond to dead time of 29, 32, and 31 ns for B, V, and R bands, respectively (plotted as filled circles, empty circles and triangles).

The photometer control software was slightly modified for this experiment. A new block was added in order to estimate the statistical parameters of the signal with periodic switching of the apertures. Each full measurement consists of N cycles through all 8 apertures, with elementary integration time T for each aperture. We typically choose $T = 1$ s (1000 data points), and $N = 26$ (4 minutes for the full measurement, to be compatible with GSM and DIMM data rate). Time lost for aperture switching is 12%.

Real-time signal processing can be schematized as follows:

1. For each 1000 data points (collected simultaneously in 3 channels) the mean values, dispersions and covariances are computed.

2. These statistical parameters are corrected for photon counting non-linearity.

3. The statistical parameters of the scintillation (dispersions and differential dispersions) are computed, with photon noise removed.

4. These parameters are accumulated during the measurement cycle. Their average value is displayed and written to the output file after completion of the cycle.

This algorithm suppresses the slow signal changes due to the star displacement in the focal aperture and transparency variations. After each 4-min measurement the centering of the star in the aperture was controlled.

The correct functioning of the hardware and software was controlled by measurements of the constant light source (LED) at fluxes similar to the actual ones. Data on Jupiter scintillation (which is extremely small) were also taken. These test data are not included in the data files.

2.3.4 Correction for counting statistics

We used bright stars α Lyr and α Cyg. Photon counting rate was high, and it was necessary to correct for the non-linearity. The technique used is described in Kornilov & Pogrosheva, 1990, and is based on the study of the statistics of the Poisson flux, which is itself sensitive to nonlinearity. A simple first-order correction was applied, which is valid for the fluxes less than $3 \cdot 10^6 s^{-1}$. For Poisson statistics with dead time the true count rate n, its variance σ^2 and covariance Cov are related to the measured quantities (same symbols with $'$) and the non-linearity parameter τ in the following way:

$$
\begin{aligned}
n &= n'(1+n'\tau) \\
\sigma^2 &= \sigma^{2'}(1-2n'\tau)^{-2} \\
Cov &= Cov'(1-2n'_1\tau_1)^{-1}(1-2n'_2\tau_2)^{-1}.
\end{aligned} \tag{5}
$$

The deviation from the Poisson law, $\sigma^{2'}/n'$, is plotted in Fig. 4 against the measured flux n'. These data were taken on July 24. The slope corresponds to the non-linearity parameters τ ("dead time") of 29 ns, 32 ns, and 31 ns for B, V, and R channels, respectively.

On the night of July 23 the pulse amplifier in the B channel was damaged. Measurements were still taken and later corrected for the actual non-linearity parameter $\tau = 240$ ns, but the data involving B channel should be considered as unreliable for this night.

Another important parameter is the non-poisson coefficient $p = \sigma^2/ < n >$ for $< n >$ close to 0 (cf. Fig. 4). In the ideal world it must be equal to 1, but in fact it can deviate from 1 for various reasons (afterpulses, ringing, interference, etc.). Coefficients p are used in calculating the intensity variance s^2 from count variance, and its error Δp leads to the error of $\Delta p/ < n >$ in s^2. For low fluxes (e.g. measurements with apertures 1 and 2) this coefficient must be known with a precision of 0.01 or better. We obtained the values of p of 0.997, 0.994, and 1.002 for B, V, and R channels, respectively. They are measured with precision of 0.003.

The transformation of the measured quantities to the scintillation statistics was done as following. Let n be mean flux from star and background together and b be mean for background only. Then the normalised scintillation index s^2 is calculated as

$$
s^2 = \frac{\sigma^2 - np}{(n-b)^2}, \tag{6}
$$

were p is non-poisson parameter of the photometric device. The dispersion of differential scintillation (see next section) in two channels A, B is:

$$
\sigma_d^2 = s_A^2 + s_B^2 - 2\frac{cov_{AB}}{(n_A - b_A)(n_B - b_B)}. \tag{7}
$$

2.4 Differential scintillation measurements

2.4.1 Optical scheme of the DASS instrument

Another instrument was an experimental device for testing the new technique of seeing estimation from differential scintillation (Tokovinin 1998). We call it DASS (Double Aperture Scintillation Sensor), or prototype. It was built using the pre-fabricated mechanical parts of the 4-channel photometer, and looks much the same. The pulse counting and data acquisition electronics are identical to those of the SP1. Instead of 4, DASS contains only 2 photomultipliers, which can measure the light flux from the 2 parts of the telescope pupil simultaneously in a single color (V band). One PM measures the light I_1 in the circular aperture with a central obscuration ϵ, while the second PM measures the flux I_2 in the central part of the same aperture.

A simplified optical scheme of the DASS is given in the Fig. 5. Light beam from the telescope passes through the focal aperture wheel 1, and the lens 2 (focal length 160 mm). Pupil image is formed at the second wheel 4 with pupil apertures. Then the beam is deflected by the prism 5.

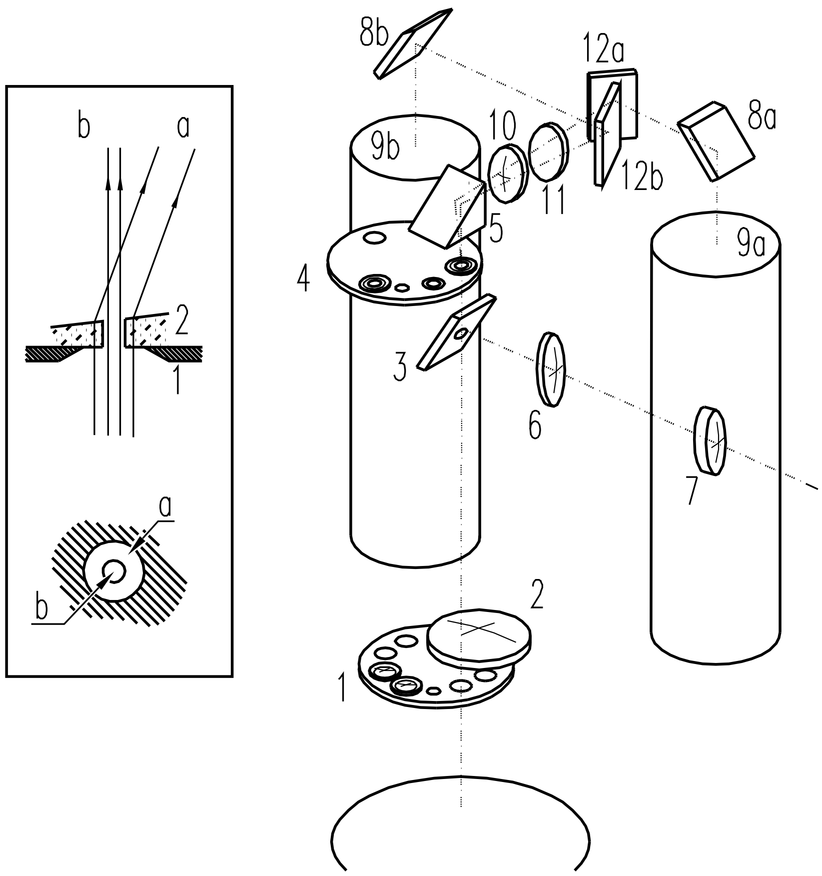

Figure 5: The optical scheme of the prototype Double Aperture Scintillation Sensor, DASS (see text).

Lens 10 reimages the focal aperture near the separating mirrors 12a and 12b, preceded by a V-band green filter 11. Then the two beams are deflected by mirrors 8a, 8b to the photocathodes of the PMTs 9a, 9b. Only part of the pupil is admitted through the hole in the mirror 3, the rest is used for viewing the star with the reimaging lens 6 and the ocular 7 of the viewer.

Double aperture is defined by a small circular prism with a hole mounted on the focal aperture wheel. As shown in the inset of Fig. 5, the central part of the beam (b) passes through the hole without deflection, while the circular part (a) is deflected by the prism. Thus, two separated images of the focal aperture are formed near the mirrors 12ab. Three double apertures of different diameters could be selected. Their central obscuration ratio is near 0.5. The diameters of the apertures (as projected onto telescope pupil plane) are:

Aperture No.	1	2	3
Diameter, cm	3.82	10.98	5.75

For the measurements of the isoplanatic angle with DASS the double aperture is replaced by the annular aperture ($D = 10$ cm, $\epsilon = 0.4$) identical to that of SP1. Only one PM is then used.

2.4.2 Calculation of seeing

The differential dispersion σ_D^2 is calculated as

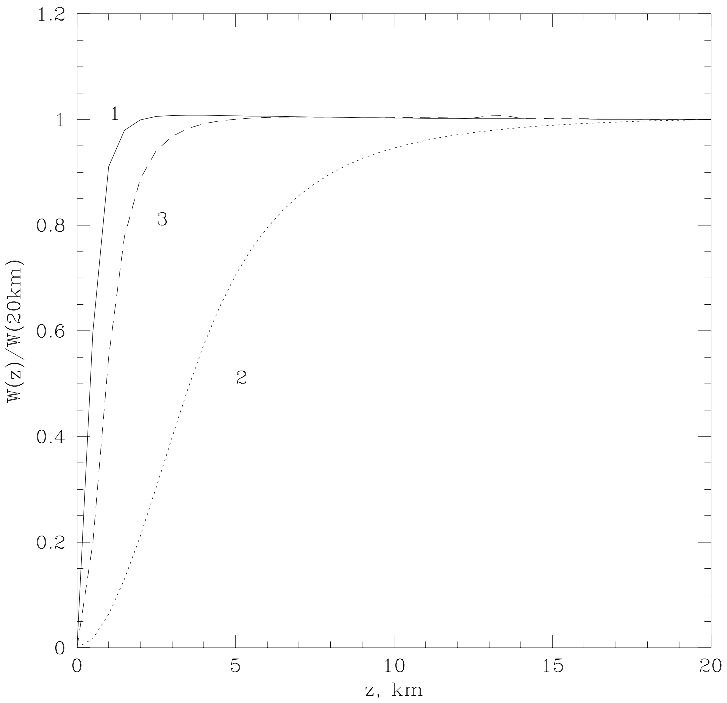

Figure 6: Weighting functions of the double apertures used in DASS (normalized to their value at 20 km) are plotted in full, dotted, and dashed lines for apertures 1, 2, 3 (aperture diameters are 3.8, 11, and 5.8 cm).

$$\sigma_D^2 =< (\Delta I_1/ < I_1 > -\Delta I_2/ < I_2 >)^2 >, \tag{8}$$

where $\Delta I_1 = I_1- < I_1 >$ is the fluctuation of the intensity. The Poisson photon noise is taken into account using the appropriate model of photon counting statistics with dead time correction, as in SP1. It can be shown (Tokovinin 1998) that the differential dispersion σ_D^2 is proportional to the integral of C_n^2 over altitude with a weighting function which grows at small altitudes and then saturates at a constant level for altitudes greater than the Fresnel radius of the inner aperture. The DASS weighting function is calculated using the Eqs. 1,2 with a modified aperture factor

$$A(f) = \left[\frac{2J_1(fD/2)}{fD/2} - \frac{2J_1(\epsilon f D/2)}{\epsilon f D/2} \right]^2 (1-\epsilon^2)^{-2}. \tag{9}$$

These functions for the three DASS apertures and $\lambda = 550$ nm are plotted in Fig. 6. Thus, σ_D^2 can be used to measure the contribution of the upper atmosphere to the total seeing. A C_n^2 integral (including the weighting function) can be converted to seeing angle β by the formula

$$\beta = K_\beta (\sigma_D^2)^{0.6}, \tag{10}$$

where the coefficient K_β is related to the weighting function value W_0 in its saturated part:

$$K_\beta = 5.307 \lambda^{-1/5} W_0^{-3/5}. \tag{11}$$

These coefficients are 8.393, 3.602, and 5.544 arcseconds for apertures 1, 2, 3, respectively. Here account is taken of the fact that σ_D^2 is measured at 550 nm, but seeing at 500 nm is calculated.

Seeing in the whole atmosphere can be also measured using this principle, if the double aperture is placed not in the pupil plane but in the plane corresponding to some altitude $-H_0$

below the ground. We make use here of the so-called "Generalized SCIDAR" concept (Fuchs et al., 1998). If the weighting function is already saturated at H_0, a good estimate of the C_n^2 integral in the whole atmosphere (and hence seeing) is obtained. To test this idea, we can install in the telescope focal plane additional lenses with focal lengths of 30 and 15 mm, which provide the virtual heights H_0 of -2 and -4 km, respectively. For apertures 1 and 3 the weighting function already saturates at 2 km, while H_0 of -6 km is required for correct seeing measurements with aperture 2. Aperture 2 is useful for upper atmosphere monitoring.

The effective height of turbulent layers in the free atmosphere can be estimated in the following way. The scintillation index in the small (inner) aperture s_2^2 is approximately proportional to the altitude of the turbulent layer. The integrated intensity of the layer is given by the σ_D^2. So, the "effective height" of the layer h_{eff} can be defined as

$$h_{eff} = h_* s_2^2 / \sigma_D^2, \tag{12}$$

where the coefficient h_* is equal to 0.59, 4.50, and 1.22 km for apertures 1, 2, 3, respectively. This is only a crude estimate, but it can be helpful in understanding the localization of the turbulence in free atmosphere.

2.5 Additional data

The meteorological parameters (temperature, wind direction and speed at ground level) were measured by the DIMM team regularly, at the beginning of each hour.

Also, I. Khamitov have kindly provided the image quality at the 1.5 m telescope, as measured on the CCD frames taken with few minutes exposure time. The IRAF task *imexamine* was used.

3 Organisation of the measurement campaign and data review

It was agreed that for budgetary and logistic reasons the duration of the joint measurements set must be around 10 days. The mission dates were fixed definitively during the INTAS meeting in May 1998 in Moscow. We selected July as being representative of the best observing period at Maidanak, i.e. from mid-summer to early autumn. The probability of good weather for this period is very high.

Part of the Tashkent team arrived at the site on July 5, and assured the construction of the GSM pier. Moscow team arrived at Tashkent on July 14, and A. Ziad (Nice team) - a day earlier. The same day a customs clearance of the GSM equipment (4 cases, total weight 350 kg) was obtained, and the joint team parted for Kitab, which is an intermediate stop-over base for Maidanak, as well as an observatory itself. We reached Maidanak on July 15th, in the evening. In the original planning this night was reserved for tests but it was lost. However, on July 16 the unpacking of GSM went on smoothly, and it was fully operational in the evening. The scintillation equipement was tested on the night of July 16. During July 17-19 the scintillation measurements were made with the prototype (DASS), and during July 20-25 the SP1 was used.

Our mission started in the conditions of stable weather with clear sky and good seeing, which persisted during the first 8 nights (July 16 - 23). Then, on July 24, 2 hours were lost due to cloud passages. On the night of July 25 only few GSM observations were made, because of

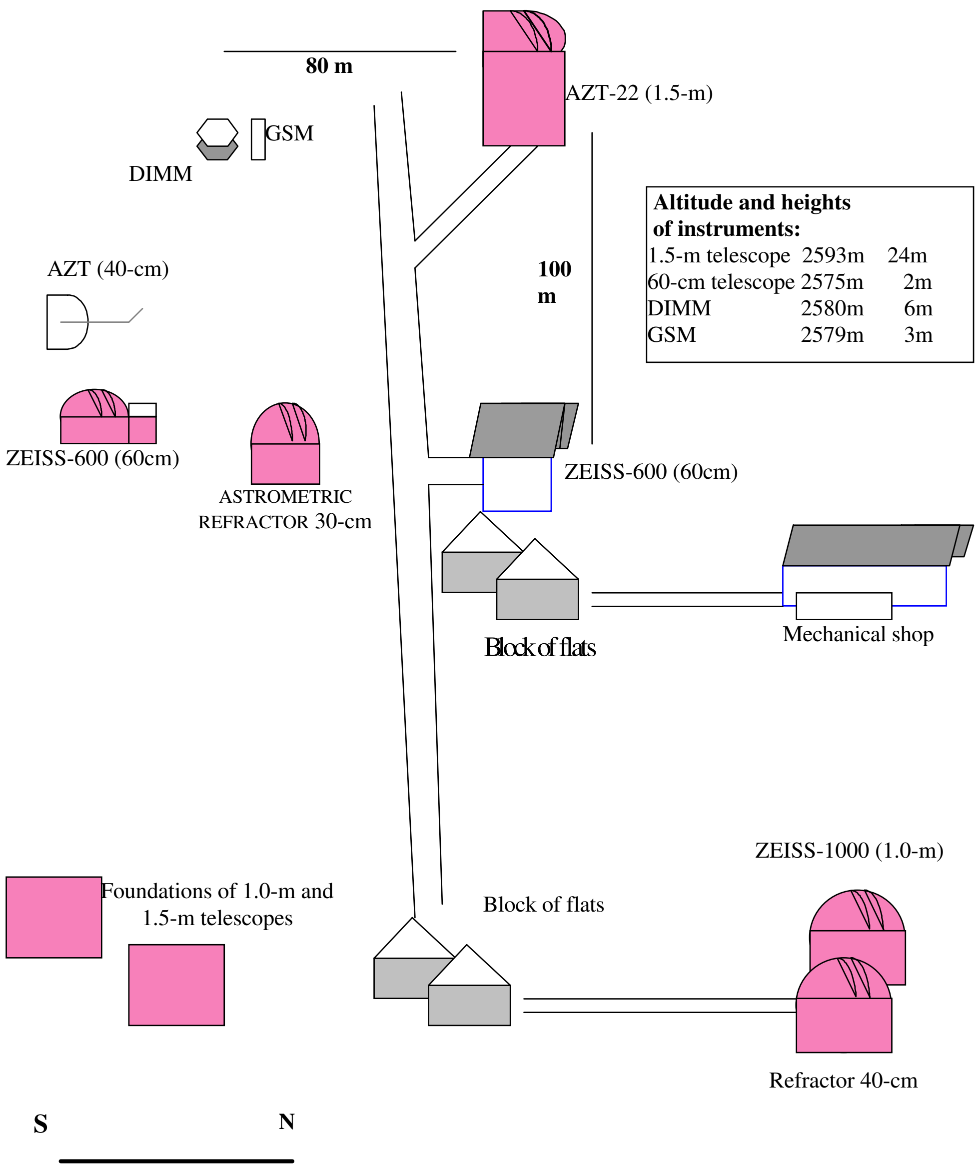

Figure 7: The schematic plan of the Maidanak Observatory. The altitudes above sea level and heights above the ground are given for the telescopes and instruments used in this campaign.

the fog and associated humidity (the previous day was rainy). This last night is considered as lost due to weather, although the scintillation and DIMM measurements were taken as planned in its second half. In summary, we had 8 clear and 2 partially clear nights out of 10.

GSM equipment was packed during the night of July 25. A. Ziad and Y. Tillaev left the site on July 26, and the rest of the team on July 28.

In Fig. 7 we give the schematic plan of the Maidanak site, showing the location of the telescopes, general facilities and site-testing equipement.

A Table 3 below summarizes the number of measurements collected during this campaign, as well as the number of hours T covered by the joint DIMM-GSM data each night. Median seeing β for each night is also given, as well as the median isoplanatic angle θ_0 and $\mathcal{L}_0$ (all from GSM data).

Table 1: Data summary

Date	Night	T, h	N_{DIMM}	N_{GSM}	N_{ISO}	$\beta_{\rm med}$ arcsec.	$\theta_{0\rm med}$ arcsec.	$\mathcal{L}_{0\rm med}$ m
16	1	4.4	83	69	3	0.96	2.02	32.6
17	2	7.0	116	100	63	0.58	2.49	27.2
18	3	4.7	54	99	558	0.74	2.24	22.6
19	4	6.2	75	96	652	0.52	3.49	26.2
20	5	7.4	111	104	0	0.53	3.43	23.2
21	6	7.3	113	101	68	0.63	2.48	27.3
22	7	6.9	99	99	86	0.87	2.41	34.6
23	8	7.4	87	103	85	0.74	2.52	22.8
24	9	7.6	74	79	62	0.79	1.79	22.7
25	10	0.5	?	7	47	1.21	1.14	25.0
Total		58.9	812	850	1625	0.68	2.48	25.9

The median seeing was $0.68''$ from GSM data or $0.64''$ from DIMM data. The $\mathcal{L}_0$ values are typical of other GSM missions: it's average is 31.5 m, median is 25.9 m. Finally, the mean isoplanatic angle θ_0 is $2.57''$ (GSM data). General behavior of outer scale, seeing and isoplanatic angle during the 9 nights of the mission is illustrated in Fig. 8.

The full tables containing the results of this campaign are provided in the electronic form as a supplement to this report. Below we give the analysis of these data. All atmospheric parameters are reduced to observations at zenith at the wavelength of 500 nm. A short description of each data set follows.

3.1 DIMM data

The measurements of seeing with DIMM were taken continuously each 4 minutes. The seeing is an average of longitudinal and transverse estimates, corrected for the finite exposure time. The moments UT given in the data files correspond to the *end* of exposure.

3.2 GSM data

Standard data were obtained from the 2-minute acquisitions taken every 4 minutes. The data file contains the date, UT moment of the *start* of exposure, instrument configuration label ('St' for standard), exposure time in seconds, source code 'aumi' (Polar Star), zenith angle, flux, and, finally, the measured seeing in arcseconds, outer scale in meters and isoplanatic angle in arcseconds.

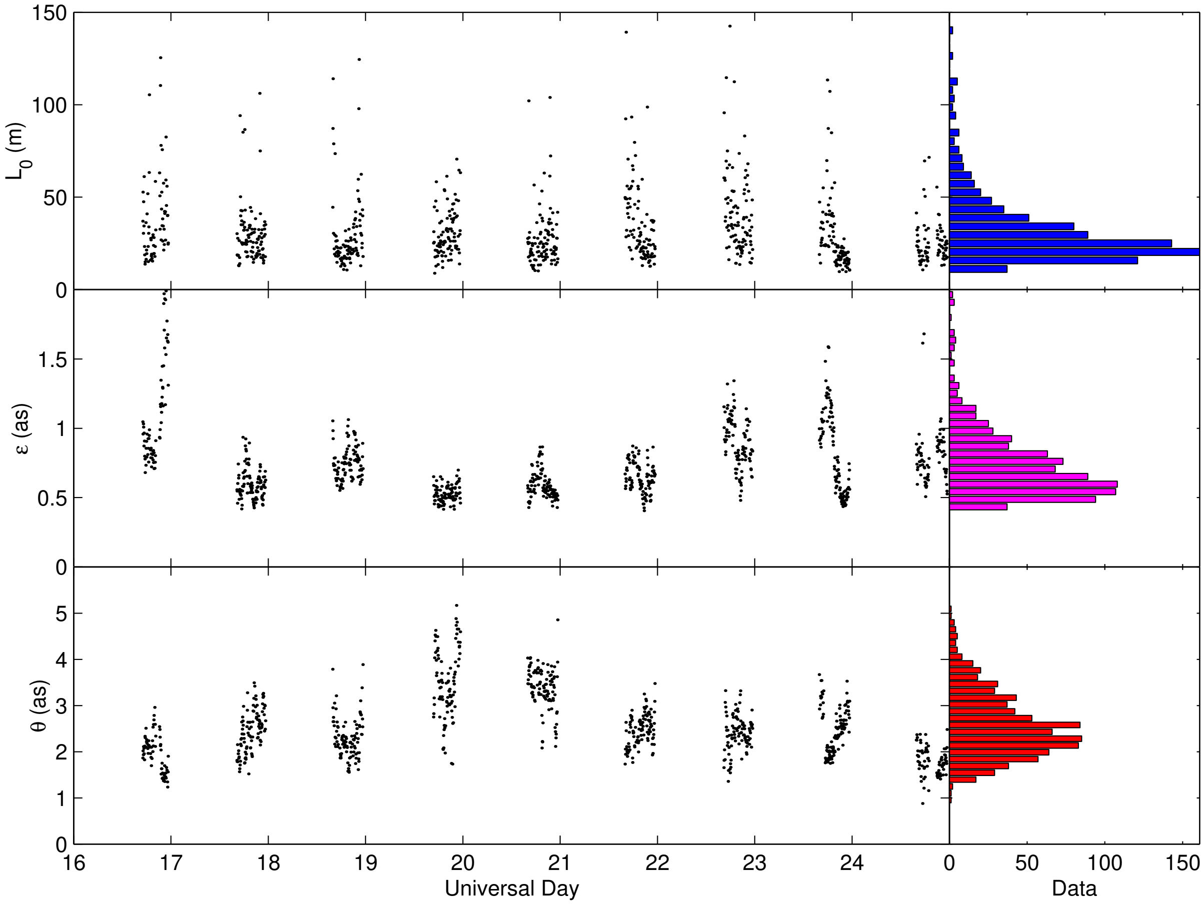

Figure 8: Summary of the GSM data for the Maidanak mission: temporal evolution of the outer scale (top), seeing (middle), and isoplanatic angle (bottom). In the right pannels the histograms are given.

3.3 Scintillation data

The measurements of the scintillation index with the 4-channel photometer (SP1) are given in the multicolumn tables (*.TBL files). Each line contains the UT time, air mass, and, for each of the 8 apertures, the following parameters are given: flux in B, V, R channels, scintillation indices s^2 in B, V, R, and differential scintillations in BV, BR, VR (the total of 74 columns). These data are not reduced to zenith.

In Fig. 9 we give as an example the temporal evolution of the scintillation index s^2 for apertures of 2.66 cm (filed circles) and 10.41 cm (empty circles) for all 6 nights (corrected to zenith). It can be seen that during this period the scintillation index gradually increased, probably because the atmospheric front was approaching. In Fig. 10 the evolution of the ratio of scintillation indices in 2.66 and 10.41 cm apertures and in 2.66 cm and 6.91 cm apertures is displayed. The comparison of the two figures shows that the ratio of scintillation indices behaves differently from the indices themselves, and reflects the changes in the effective height of the turbulent layers. On the night of July 25, when scintillation was the strongest, the ratio of scintillation indices in various apertures was very stable, indicating that the effective height of the dominant layer did not change during the night.

Isoplanatic angles are calculated from the scintillation index measured with the annular

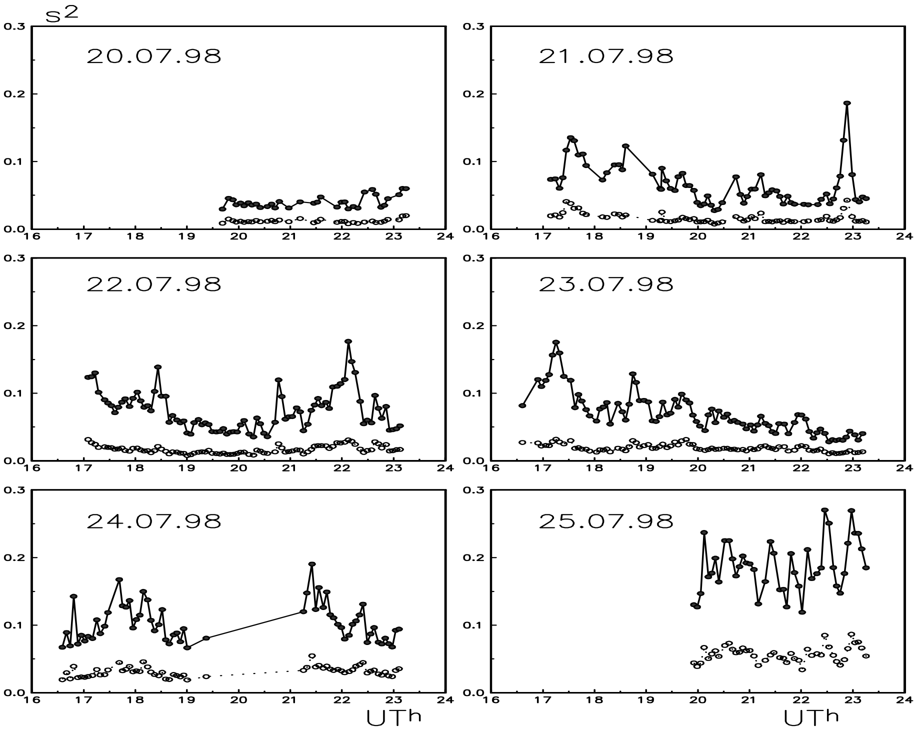

Figure 9: Temporal evolution of the scintillation index at zenith for apertures of 2.66 cm (filed circles) and 10.41 cm (empty circles). Gaps in data on July 24 and 25 are due to clouds. Scintillation indices are reduced to zenith.

aperture using Eq. 4. Files ****iso.dat contain UT in the first column, air mass in the second column and θ_0 in the remaining column(s). For the nights of July 17, 18, 19 the measurements were taken with the DASS in the V band only. On July 20 SP1 was used, but the annular aperture was not yet installed, and the first half of the night was used for tests. On July 21-25 the isoplanatic angle was measured simultaneously in 3 colors, so colums 3, 4, 5 contain θ_0(500 nm) from B, V, and R band data, respectively. Generally a very good agreement between these 3 independent estimates is observed, except on July 23 when the B channel was damaged (Fig. 11).

Files with the DASS results contain UT in the first column (which corresponds to the center of integration period), air mass in the second column, scintillation indices in the outer (1) and inner (2) apertures, differential scintillation in the 4th column and the seeing angle β calculated from the differential scintillation. The apertures (1, 2, 3) and defocusings (B, C, D for 0, -2 and -4 km) are coded as file extensions, e.g. 170798.B1 refers to the measurements with aperture 1 without defocusing.

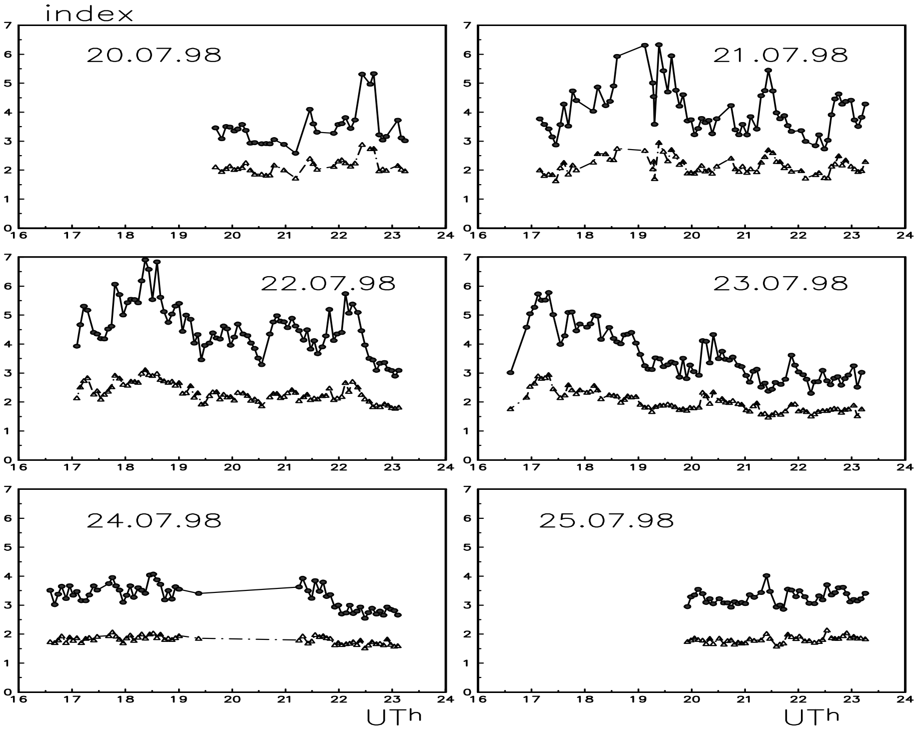

Figure 10: Temporal evolution of the ratio of scintillation indices in 2.66 and 10.41 cm apertures (filled circles) and in 2.66 cm and 6.91 cm apertures (empty triangles).

Figure 11: Isoplanatic angles at $\lambda = 500$ nm calculated from the simultaneous scintillation data in B, V, and R colors (full, dashed and dotted lines, respectively) obtained with SP1 on July 22. A very good agreement can be seen.

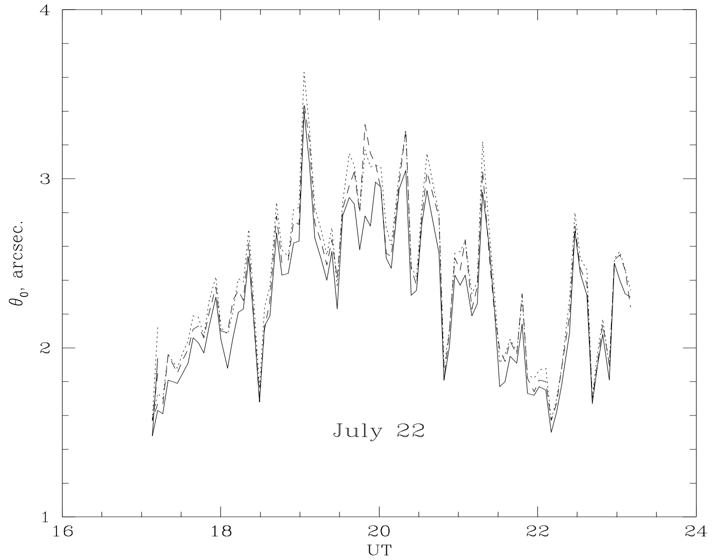

4 Data analysis

4.1 Wavefront velocities from GSM data

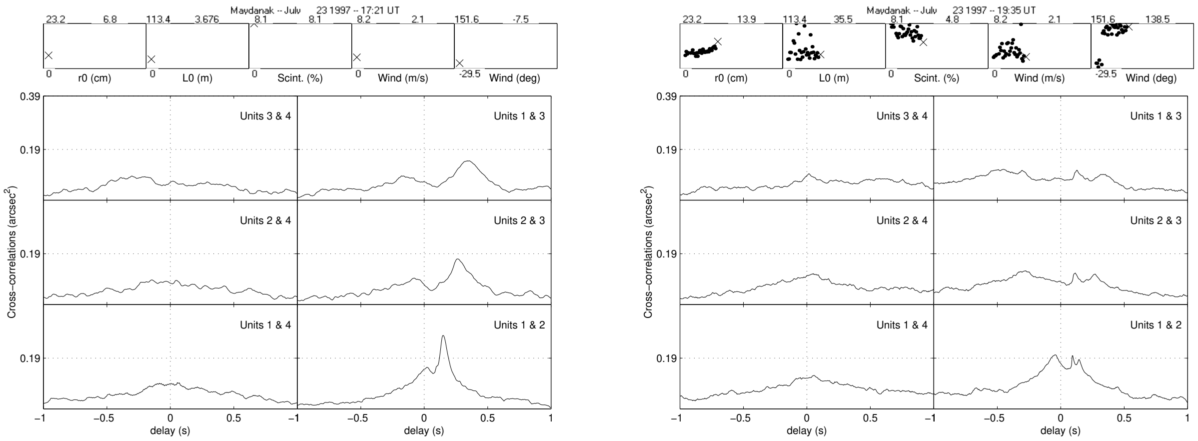

Figure 12: The examples of cross-correlation functions of the AA fluctuations at the 6 GSM baselines for the night of July 23, at 17:21 UT (left pannel) and 19:35 UT (right pannel). A complex layer structure was present on this night as evidenced by multiple peaks in cross-correlations.

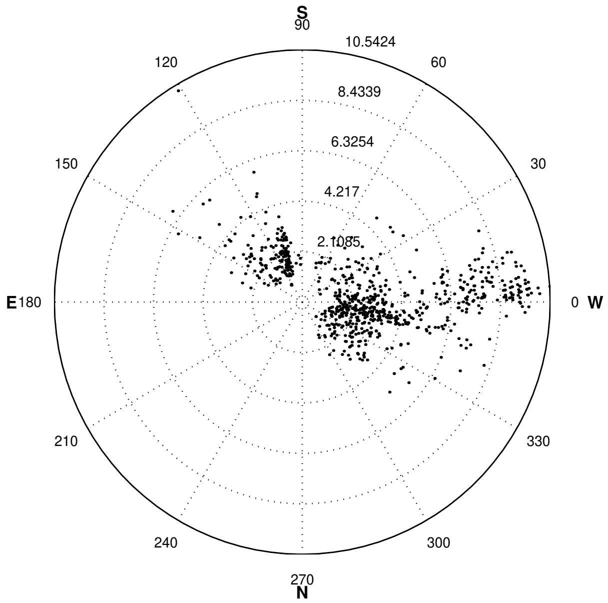

Figure 13: Direction and velocity of the wavefront for the whole mission dataset, plotted as a polar diagram. The western wind of low to moderate velocity was predominant, with south-east winds being less frequent.

The wavefront speeds (velocities and directions) of the predominant turbulent layers of the atmosphere was determined from the analysis of AA temporal cross–correlation functions at all GSM baselines. The eddies carried by the winds in the layers produce several peaks in the cross–correlations. With the hypothesis of the frozen–flow, the positions of the peaks depend on the baseline and on the projection of the wind on the baseline as show by Avila et al. (1997). Practically, the positions of the highest peak is measured on the six cross–correlations. To reconstruct the wind vector, two non–parallel baselines are necessary. With the six baselines of the GSM, 11 couples of equations lead to the 11 measurements of the wind vector. The final value is the median of these. This procedure turned out to be rather robust. When several layers are present (which was almost always the case), our wavefront velocity vectors fluctuate between the values typical for each layer, because of turbulence intermittency. So, the plots of wind direction and velocity against time usually reveal the multi-layer structure quite well. A more refined analysis of the cross-correlation functions is planned in the future.

Examples of cross-correlation functions obtained on the night of July 23/24 are given in Fig. 12. Multilayer structure of turbulence is clearly apparent in these plots. It must be noted that when wind direction is parallel to the baseline the correlation peaks are much sharper than for other angles, due to a good correlation between the high-frequency components of the AA fluctuations.

The overall distribution of the direction and velocity of wavefront is given in Fig. 13. A predominant western direction is apparent. It corresponds to the planetary circulation in the free atmosphere. Very low wind speed is evident: it was less than 2 m/s most of the time, and never exceeded 10 m/s. From the inspection of night-by-night data it is clear that there was no correlation of "GSM wind" with the ground wind measured near DIMM. It indicates that the surface layer turbulence did not provide the major contribution to the total seeing. The same conclusion emerges from the more direct measurements presented in the next section.

4.2 Comparison of DIMM and GSM seeing. Role of the local turbulence.

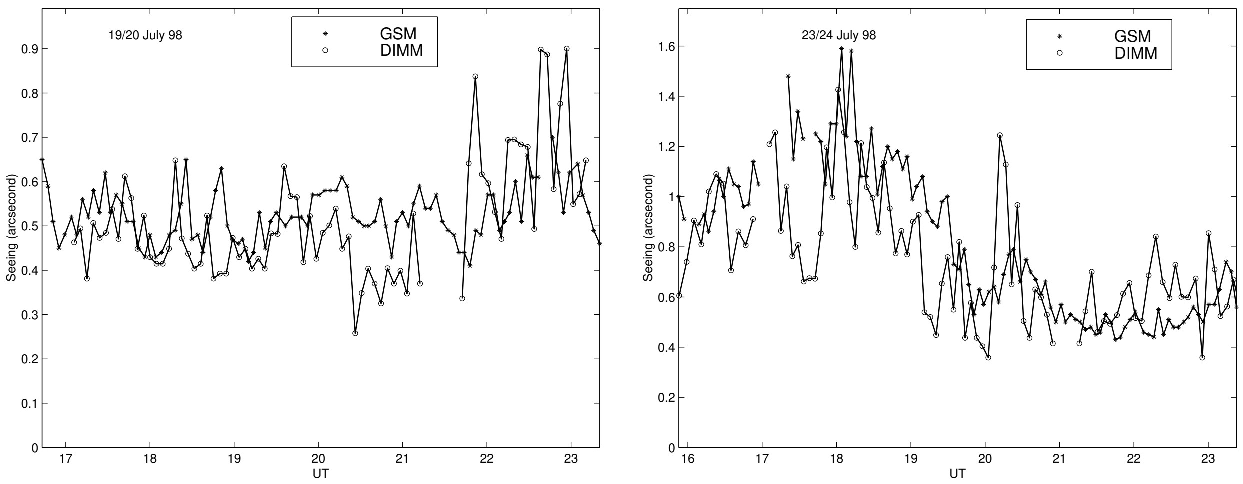

Figure 14: Seeing measured by GSM (thick line) and by DIMM (thin line) on the night of July 19 with the best seeing (left) and on July 23 with average seeing (right), when for the first 2 hours GSM units 1 and 2 were installed on the DIMM pier.

As can be seen from the Fig. 14, a good mutual agreement of GSM and DIMM seeing estimates exists most of the time. DIMM measurements show a larger scatter, explained by the small number of processed images. The 25%, 50% and 75% levels of the cumulative seeing distribution as measured with GSM are 0.56, 0.68 and 0.84 arcsec. The corresponding values for DIMM are 0.52, 0.64 and 0.82 arcsec.

Two possible reasons of discrepancy have been previously identified in course of the La Silla mission:

1) Temporal averaging in DIMM with its 10 ms exposure time. This effect is now corrected by the interlaced exposure technique. Seeing at Maidanak is likely to be slower than at La Silla. So, this effect was not relevant for our mission.

2) Different height of the 2 instruments above the ground. Compared to La Silla, we increased the height of GSM to 3.4 m above ground to minimize this difference. Also, the effect of the surface layer was controlled because module 4 of GSM was installed at a lower height of 1.9 m.

The integral J_{SL} of C_n^2 in the surface layer from 1.9 to 3.4 m was estimated from the difference of seeing measured by identical modules 3 and 4. If r_{03} and r_{04} are Fried radius estimates in cm, then J_{SL} can be expressed as

$$J_{SL} = 3.225 \cdot 10^{-11} (r_{04}^{-5/3} - r_{03}^{-5/3}) \;\; [m^{1/3}]. \quad (13)$$

It turns out that random errors in the r_0 estimates limit the precision of the individual J_{SL} estimates at a level of about $1 \cdot 10^{-13}$. However, the systematic trends in $J_{SL}(t)$ can be readily detected. The nightly mean values of J_{SL} were calculated, and are presented in Table 2. The seeing degradation corresponding to the surface layer alone, β_{SL}, is also calculated. Median nightly values of seeing β_{med} are given for comparison. The relative contribution of the surface layer to the total C_n^2 integral is given in the last column, estimated as $(\beta_{SL}/\beta_{med})^{5/3}$. Its typical values are less than 20%.

Since July 21 modules 3 and 4 were swapped, to make shure that their calibration did not contribute to the systematic seeing difference. Indeed, *negative* mean values of J_{SL} obtained on July 21 and 22 signal that J_{SL} was probably underestimated after module swapping, and overestimated before because of slight calibration bias between the modules 3 and 4.

Table 2: Ground layer turbulence summary

Date	Night	β_{med}, arcsec	$< J_{SL} >$, $10^{-14}\ m^{1/3}$	β_{SL}, arcsec	J_{SL}/J_{tot}, %
16	1	0.95	24.0	0.52	37
17	2	0.58	8.9	0.29	31
18	3	0.74	5.5	0.22	13
19	4	0.52	4.0	0.18	17
20	5	0.56	2.1	0.12	8
21	6	0.63	-4.0	-	-
22	7	0.87	-0.27	-	-
23	8	0.73	3.4	0.16	8
24	9	0.78	4.5	0.19	10

The most dramatic surface layer effect was found in the end of the first night (Fig. 15, left). Surface layer alone caused seeing degradation up to 1.4″! This corresponded to the period of the worst seeing measured throughout this campaign. Unfortunately, DIMM was not operational during this time. A more typical example of two nights with good seeing is shown in the right pannel of Fig. 15. The surface layer contribution is barely apparent, its net effect being on the level of $1 \cdot 10^{-13} m^{1/3}$ (0.3″ seeing) or less. It is clear that such turbulence can contribute to

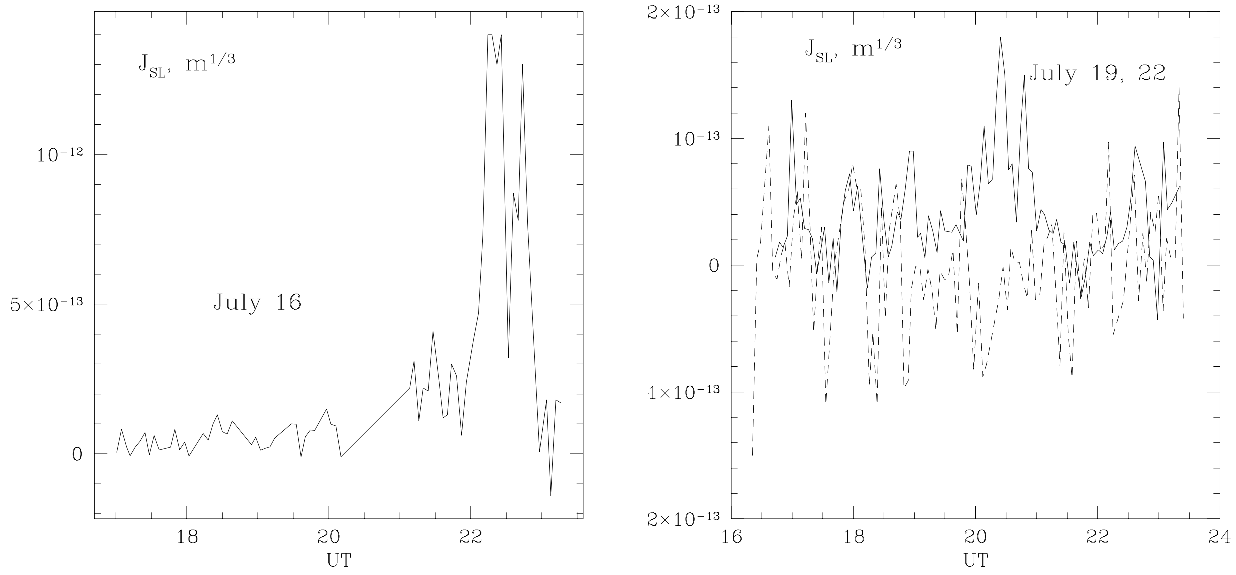

Figure 15: The evolution of the surface layer turbulence J_{SL} on three nights. On July 16 (left) very strong surface layer turbulence was present in the second half of the night. On the nights of July 19 and 22 (right, full and dashed lines respectively) with good seeing little turbulence in the surface layer was detected.

GSM-DIMM difference only weakly during the periods of excellent seeing. We estimate now this contribution in a more quantitative way.

From the paper of Gouryanov et al. (1992) it follows that the $C_n^2(h)$ profile in the surface layer at Maidanak can be well approximated by the h^{-2} law. Thus, a C_n^2 integral from height h_1 to h_2 is proportional to $h_1^{-1} - h_2^{-1}$. Using this law, we can infer that the integral from 3.4 to 30 m is $1.12 J_{SL}$, and for the 3.4-6 m layer it is $0.55 J_{SL}$. Thus, J_{SL} as defined above is actually a good estimate of the surface layer contribution to GSM seeing, and an overestimate of the possible DIMM-GSM seeing difference due to different heights. If J_{SL} contributes about about 20% to the total GSM seeing, the DIMM-GSM systematic difference must be around $0.9^{3/5} = 0.94$. It is exactly the ratio of the median seeing measured by both instruments! If we define the upper height of surface layer as 30 m, its contribution to DIMM seeing is $0.57 J_{SL}$. Increasing the height of a site testing instrument from 3.4 m to 6 m does not eliminate the surface layer completely, but reduces its contribution by a factor of ≈ 2.

DIMM and GSM observed different stars (a star near zenith and Polaris), and hence sampled different volumes of the atmosphere. Correction of the GSM seeing to zenith was not very large, $(\sec 51^o)^{0.6} = 1.32$. In some special circumstances, however, the difference of the optical paths was indeed significant because of the local orographic turbulence. When slow wind was blowing from the North, our instruments could be affected by the turbulent lee of the telescope dome and its surroundings. In this case GSM suffered much more than DIMM, because it looks to the North. Apparently, such a situation happened on July 23 in the evening, when we decided to compare GSM and DIMM in a more direct manner and installed for 2 hours the GSM units 1 and 2 on the DIMM pier (Fig. 14). Seeing measurements from the same location turned out to be different! Later, when GSM was back to its standard configuration, this difference disappeared.

Our experience shows that at a site with good seeing like Maidanak, the local turbulence becomes important. Depending on wind direction and velocity, surface layer may contribute to seeing degradation, especially in a location which is not on the very top of the mountain, like DIMM or a 60 cm telescope.

4.3 Comparison of θ_0 measured by GSM and SP1

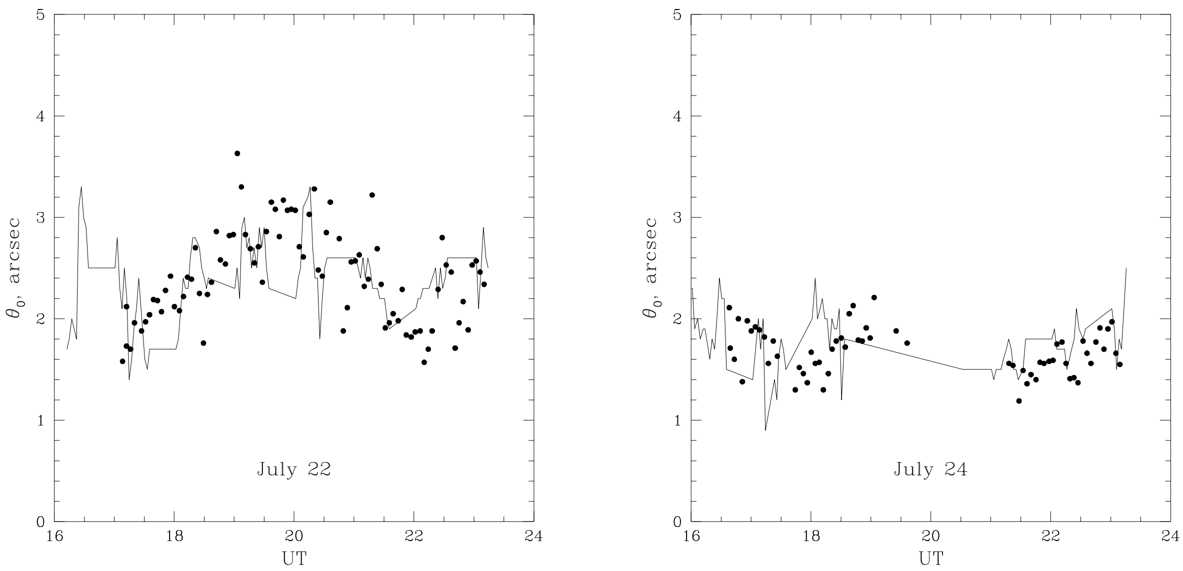

Figure 16: Comparison of the isoplanatic angle measured by GSM (line) with data from the SP1 scintillation photometer (dots) for two nights, July 22 (left) and July 24 (right), when seeing was worse and measurements were interrupted by clouds.

In Fig. 16 the θ_0 as measured by GSM is compared to the θ_0 given by SP1 for two nights. A very good agreement is seen, despite the fact that GSM was not originally designed for θ_0 measurements. A fairly large correction for zenith angle (GSM observed Polar star at $z = 52^o$, while SP observed stars near zenith) and a correction for finite exposure time of 5 ms seem now to be well justified.

Isoplanatic angles measured with DASS prototype on the nights of July 17-19 are, on the average, slightly (by $\approx 10\%$) larger than those given by GSM. We attribute this small difference to the experimental nature of the prototype.

4.4 Turbulence in the upper atmosphere from scintillation data

The three nights of measurements with the DASS prototype provided data on the integrated turbulence in the upper (free) atmosphere. Their comparison with seeing as measured by GSM gives a relative contribution of the free atmosphere to the seeing at Maidanak. We must remind that this technique is still in the experimental phase, and the results presented in this section must be considered as preliminary.

On each of the 3 nights a different aperture was used for most of the measurements. So, the meaning of the "free atmosphere seeing" β_{free} is somewhat different (cf. the weighting functions in Fig. 6). An integrated seeing was also measured by defocusing the double aperture. However, it was immediately apparent that an appreciably worse seeing was measured by DASS than by

GSM or DIMM. This is presumably because telescope and its enclosure provided most of the turbulence. Indeed, a visual inspection of the telescope pupil with a Foucault knife revealed the strong slowly moving structures typical of the dome turbulence. A tendency of improvement of the local seeing in the second half of the night was clearly seen.

In Figs. 17, 18, 19 the plots of the various seeing estimates with DASS and GSM are given for the nights of July 17, 18 and 19.

Figure 17: Comparison of the seeing measured by GSM (line) with the seeing in the upper atmosphere and at the 60 cm telescope on the night of July 17. Filled circles and asteriscs denote upper atmosphere seeing measured with double apertures 1 and 2. Empty circles - telescope seeing measured with aperture 1 and -2 km defocusing.

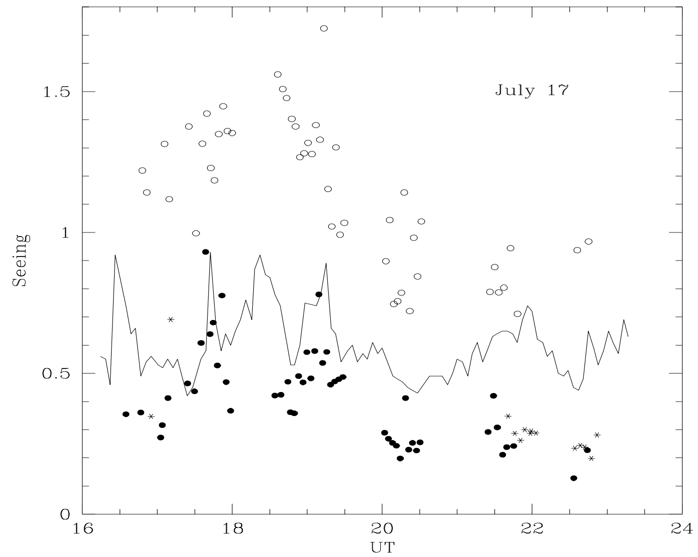

Figure 18: Same as in Fig. 17 for the night of July 18. Filled circles and asteriscs denote upper atmosphere seeing measured with double apertures 1 and 2. Empty circles - telescope seeing measured with aperture 1 and -2 km defocusing, empty squares - telescope seeing with aperture 2 and -4 km defocusing.

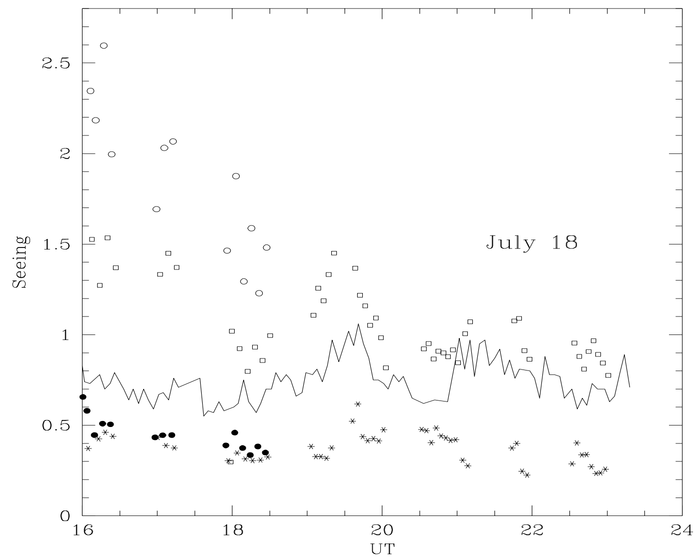

On the night of July 17 the two bursts of β_{free} (at 17.5h and 19h UT) match in time and amplitude the degradation of the total seeing β. During these short periods the free atmosphere provided a dominant contribution to seeing. For the rest of the time β_{free} is consistently smaller than β . Thus, seeing was mainly degraded by boundary layer contribution. This is particularly true for July 18. On this night a good agreement of β_{free} as measured with apertures 1 and

Figure 19: Same as in Fig. 17 for the night of July 19. Filled circles and asteriscs denote upper atmosphere seeing measured with double apertures 3 and 2. Empty circles - telescope seeing measured with aperture 3 and -2 km defocusing, empty squares - aperture 3 with -4 km defocusing.

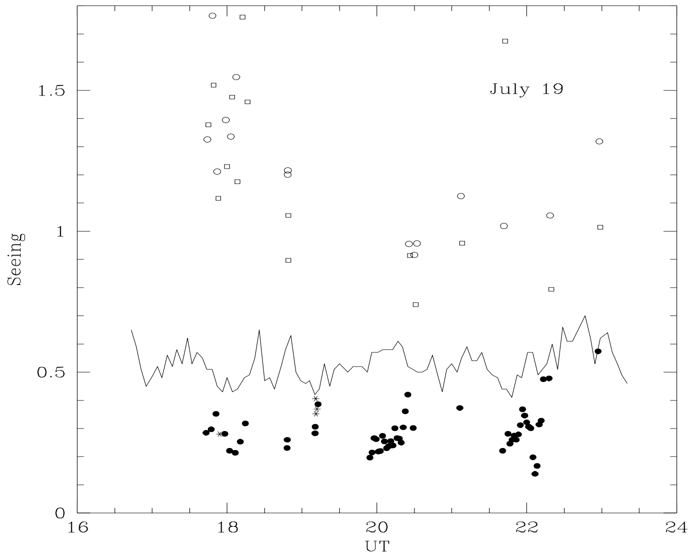

2 is seen, indicating that layers below 6 km did not contribute to free atmosphere seeing (if the C_n^2 distribution were uniformly decreasing with height, like Hufnagel profile, a much larger difference between apertures 1 and 2 would be expected). Finally, even on the night of July 19 with excellent and stable seeing around $0.5''$ the free atmosphere alone contributed less than boundary layer (the surface layer was not important, as shown above). On this night the best seeing and the largest isoplanatic angles were registered.

The effective height of turbulent layers h_{eff}, as estimated from the ratio of intensity fluctuations in small aperture to differential variance, is plotted in Fig. 20. The largest variability of h_{eff} was observed on July 17; apparently, a strong turbulence at 3 km above the summit appeared during two short periods, which increased the total contribution of upper atmosphere to the seeing. On the next night the effective height was around 8-9 km (near the tropopause) and very stable. Finally, on July 19 the effective height was 3-5 km.

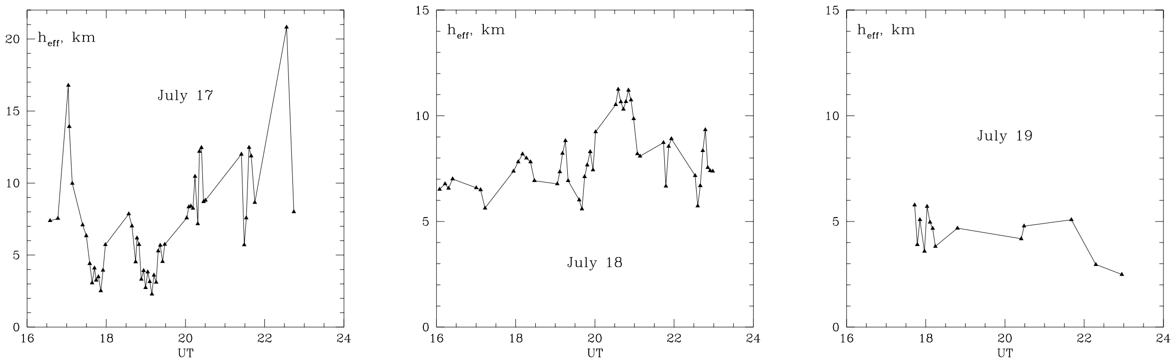

Figure 20: The effective height of the upper atmosphere turbulence h_{eff} (km) on the nights of July 17 (left), July 18 (middle), and July 19 (right).

It seems that the new technique of estimating the C_n^2 integral from differential scintillation gives a valuable complement to the traditional seeing data and helps to estimate the relative contribution of the free atmosphere to the seeing.

4.5 Seeing at the 1.5 m telescope

In Fig. 21 we compare the seeing measured at the 1.5 m telescope (reduced to zenith and to the wavelength of 500 nm) to the atmospheric seeing measured by GSM for the two nights with bad and good atmospheric conditions. Telescope seeing was typically around 1″ for good conditions, and sometimes worse. Practically no correlation with atmospheric seeing is noted. It means that despite the measures for improvement of telescope seeing (which consist mainly in air suction from the dome) the image quality at the 1.5 m telescope is still determined by local effects in the dome and tube of the telescope and/or telescope focusinf and pointing errors. Curiously, the seeing measured at the 0.6 m telescope by DASS is very similar to the 1.5 m seeing, which also improves in the second half of the night.

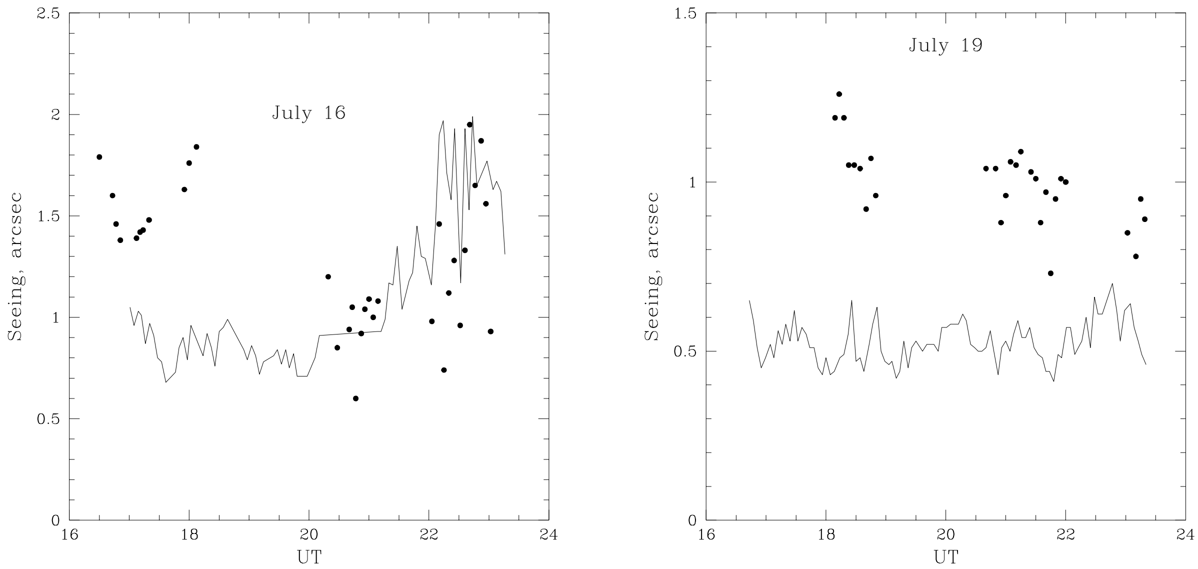

Figure 21: Comparison of the atmospheric seeing as measured by GSM (full line) and the image FWHM on the CCD exposures taken at the 1.5 m telescope (filled circles) on two nights. In the second half of July 16 night (left) a very strong surface layer turbulence was detected by GSM. So, the near coincidence of GSM and telescope seeing during this period seems to be accidental. On the night of July 19, which is also typical of other good nights, the telescope image quality steadily improves during the night, showing little correlation with the atmospheric seeing.

5 Conclusions

The main results of our campaign can be summarized as follows:

1. A good agreement between two independent seeing monitors DIMM and GSM was found, confirming the excellent average seeing at Mt. Maidanak. The median seeing for the 9 nights of our campaign was 0.64 arcseconds (DIMM).

2. The statistics of the wavefront outer scale at Maidanak was obtained for the first time. Its median value is 25.9 m, i.e. quite similar to that at the La Silla observatory.

3. Isoplanatic angle was measured at Maidanak for the first time. Median value for our campaign is 2.48″ (at 500 nm wavelength). A good agreement of θ_0 measured by GSM and SP1 photometer was found.

4. The dominant direction of the wavefront motion was from the West, and its velocity was very low, less than 2 m/s most of the time and never exceeding 10 m/s. Multilayer wavefront structure was typical.

5. Turbulence in the free atmosphere (higher than 1 km above the mountain) did not provide the major contribution to the seeing (except on rare occasions), which was hence dominated by boundary layer (the surface layer was not important either).

6. Image quality at the 1.5 telescope was dominated by local turbulence in the tube and dome and/or focusing and guiding erors.

Further measurements will be needed for better understanding of the vertical turbulence profile. This will be achieved by combining the improved analysis of stellar scintillation with the DIMM data. Next missions are planned for years 1999 and 2000.

This misssion has fully demonstrated the potential of modern optical techniques for a complete characterization of the turbulence at an astronomical site. Maidanak observatory is qualified as a promising site for high-resolution observations, which would greatly benefit from excellent seeing, little high-altitude turbulence and slow wind.

6 Acknowledgments

The efficient realization of this project would have been impossible without the aid of many people. We appreciate the help of UBAI staff in the organization of the mission support (transport, infrastructure preparation, equipment installation and operation). In particular, we want to thank Abbas Aliev for the help in GSM installation and for participation in DIMM observations and Irek Khamitov for the data on 1.5 m telescope seeing. O.Voziakova has participated in observations with SP1 and DASS.

One of the results of this campaign was the intensive exchange of experience and ideas among the participants. We all have acquired a deeper understanding of equipment operation and the underlying physics.

References

[1] Agabi A., Borgnino J., Martin F., Tokovinin A.A., Ziad A. *G.S.M.: a Grating Scale Monitor for atmospheric turbulence measurements. II. First measurements of the wavefront outer scale at the O.C.A.* Astron. Astrophys. Suppl. Ser., 1995, V. 109, P. 557.

[2] Avila R., Ziad A., Borgnino J., Martin F., Agabi A., Tokovinin A. *Theoretical spatio–temporal analysis of angle of arrival induced by atmospheric turbulence as observed with the Grating Scale Monitor experiment.* J. Opt. Soc. Am. A, 1997, V. 14(11), p. 3070–3082.

[3] Fried D.L. *Anisoplanatism in adaptive optics.* J. Opt. Soc. Am., 1982, V. 72, p. 52-61.

[4] Gouryanov A.E., Kallistratova M.A., Kutyrev A.S. et al. *The contribution of the lower atmospheric layers to the seeing at some mountain observatories.* Astron. Astrophys., 1992, V. 262, P. 373.

[5] Ilyasov S.P., Baijumanov A.K., Sarazin M., Sultanov H.B., Ehgambergiev Sh.A. *The night time seeing measurements at Mt. Maidanak with the ESO differential image motion monitor.* Pis'ma v AZh (Astronomy Letters), 1998, V. 24, accepted.

[6] Kornilov V.G., Pogrosheva T.M. *Non-traditional method for the investigation of photodetector receiver nonlinearity.* Astron. Zhourn, 1989, V. 66, P. 424-425.

[7] Kornilov V.G., Krylov A.V. *The four-channel stellar photometer for bright star observations.* Astron. Zhourn, 1990, V. 67, P. 173-181.

[8] Kornilov V.G. *Four-channel stellar photometer with dichroic beam-splitter.* Baltic Astronomy, 1998, V. 7, p. 513-524.

[9] Krause-Polstorf J., Murphy E.A., Walters D.L. *Instrumental comparison: corrected stellar scintillometer versus isoplanometer.* Appl. Opt., 1993, V. 32, P. 4051.

[10] Loos G.C., Hogge C.B. *Turbulence of the upper atmosphere and isoplanatism.* Appl. Opt., 1979, V. 18, P. 2654-2661.

[11] Martin F., Tokovinin A.A., Agabi A., Borgnino J., Ziad A. *G.S.M.: a Grating Scale Monitor for atmospheric turbulence measurements. I. The instrument and first results of angle of arrival measurements.* Astron. Astrophys. Suppl. Ser., 1994, V. 108, P. 173.

[12] Martin F., Tokovinin A., Ziad A., Conan R., Borgnino J., Avila R., Agabi A., Sarazin M. *First statistical data on the wavefront outer scale at La Silla observatory.* Astron. Astrophys., 1998, V. 336, P. L49-L52.

[13] Sarazin M., Roddier F. *The ESO differential seeing monitor.* Astron. Astrophys., 1990, V. 227, P. 294.

[14] Sarazin M. *Automatic Seeing Monitoring for Queue Scheduled Astronomical Observations.* Proc. SPIE, 1997, V. 3125, P. 366-374.

[15] Fuchs A., Tallon M., Vernin J. *Focusing on a turbulent layer: principle of the "Generalized SCIDAR".* Publ. Astron. Soc. Pacif., 1998, V. 110, p. 86-91.

[16] Tokovinin A.A., Ziad A., Martin F., Avila R., Borgnino J., Conan R., Sarazin M. *Wavefront outer scale monitoring at La Silla.* Proc. SPIE, 1998, V. 3353, P. 1155-1162.

[17] Tokovinin A.A. *A new method to measure the atmospheric image quality.* Pis'ma v AZh (Astron. Letters), 1998, V.24, P. 768-771.

7 Appendix: Night-by-night data

The next 9 pages contain the detailed plots of each night's data. The top 5 pannels represent the temporal evolution of the major wavefront parameters as measured by GSM (with the distributions of some parameters on the right side):

- Wavefront outer scale $\mathcal{L}_0$ in meters.
- Seeing angle ϵ in arcseconds (FWHM, reduced to zenith, $\lambda = 500$ nm).
- Isoplanatic angle θ_0 in arcseconds, also reduced to zenith and at 500 nm.
- Velocity module of the dominant wavefront motion in m/s.
- Direction of the dominant wavefront motion. This plot is cyclic (points at top and bottom refer to the same direction, West). Bimodal distribution of velocity or direction is a diagnostic of multilayer wavefront structure, which is also reflected in the comments.

The lowest graphs represent the evolution of ground temperature and wind speed, as measured by DIMM team each hour, and a polar diagram of wavefront wind speeds.

Finally, a verbal comment on each night is given, supplemented by the description of wavefront motion ("GSM wind") and meteo conditions.

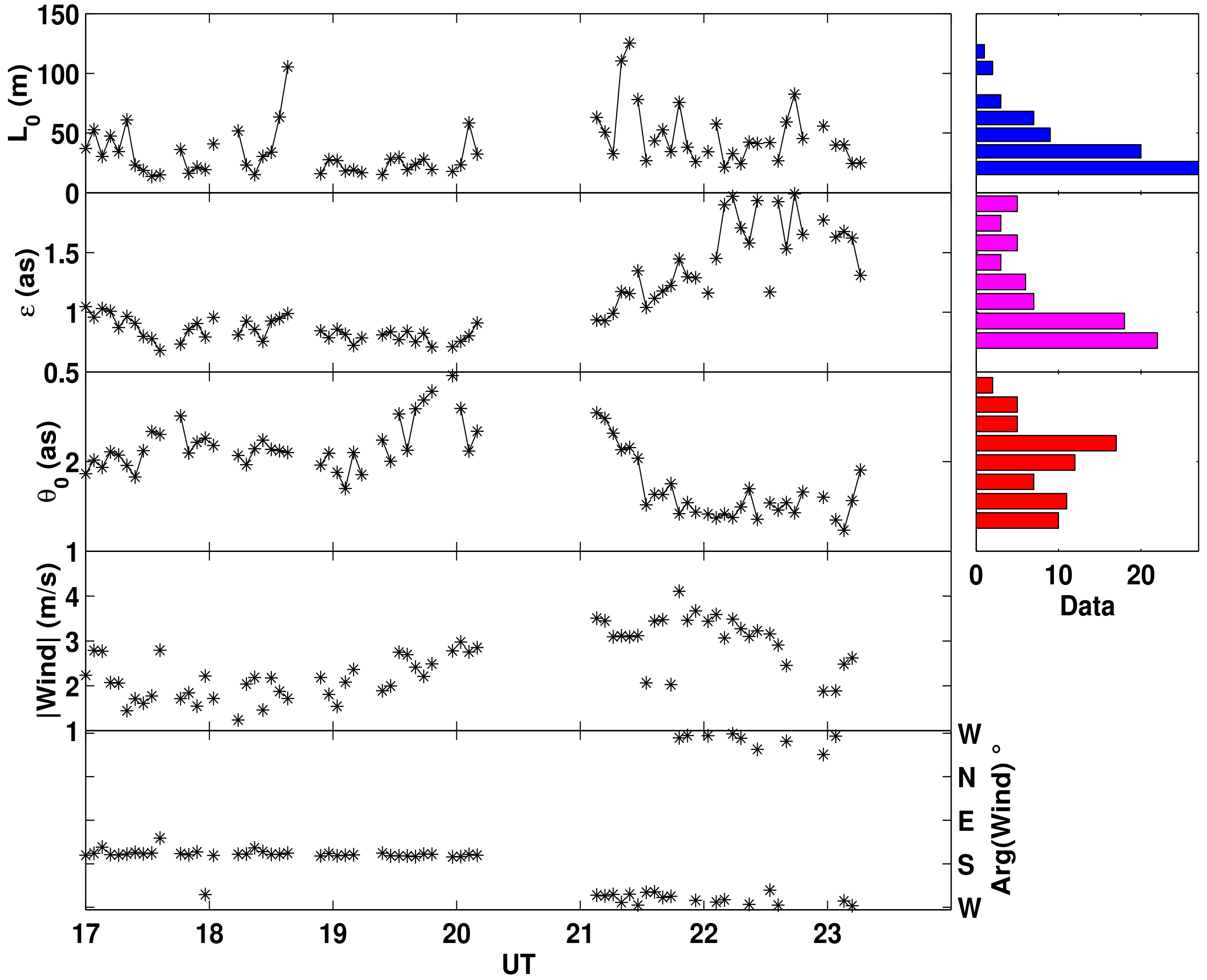

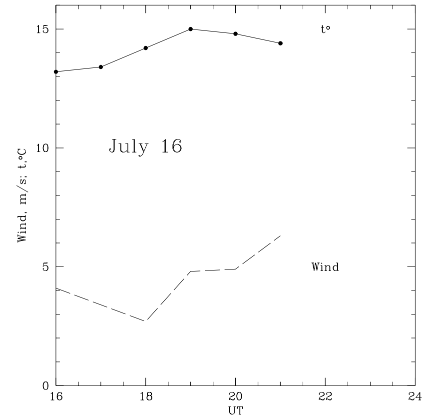

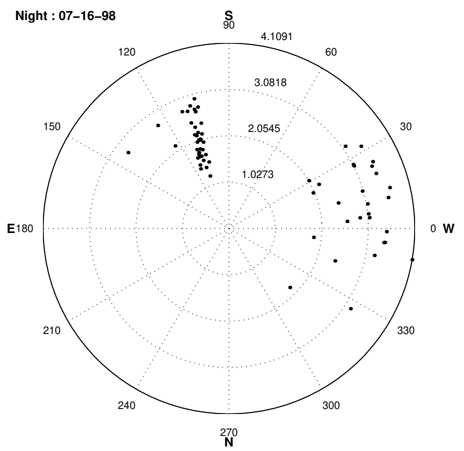

1. July 16/17

During the second half of this night DIMM was not operational due to technical problems. Very strong turbulence in the surface layer developed by the end of the night, degrading the seeing substantially. Scintillation measurements were not yet operational.

GSM-wind: Two layers were detected with winds from the West and the South, respectively. An another layer is seen on the cross–correlations but its associated peaks is never the highest. It blew approximately from the West.

Ground wind: E until 18h, then SE. Sky: clear.

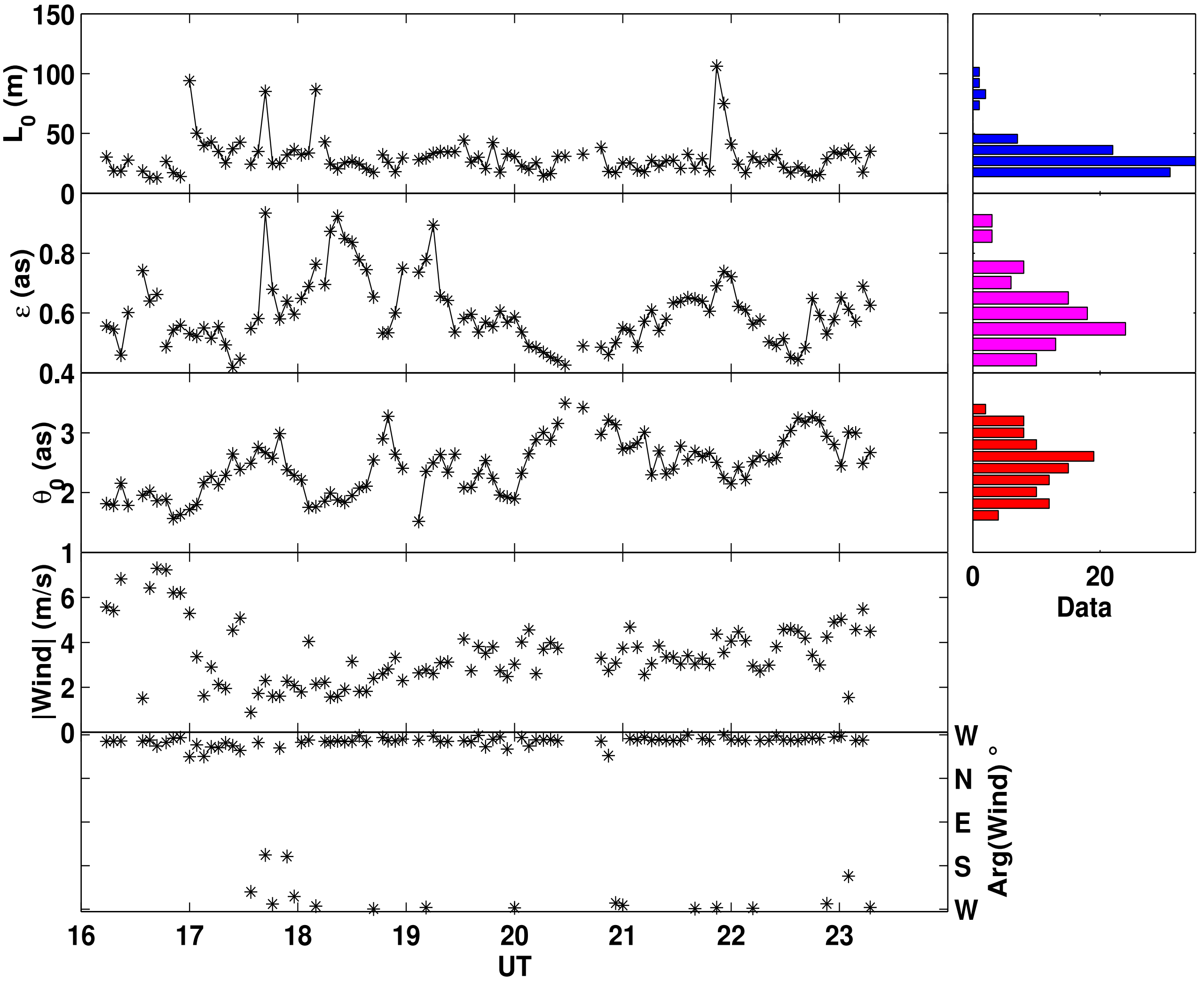

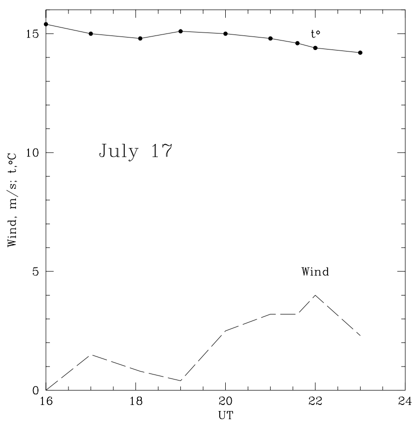

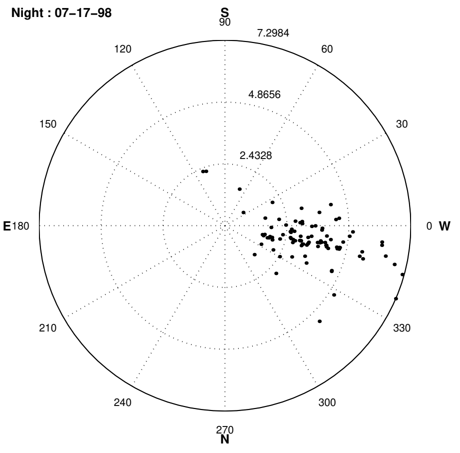

2. July 17/18

Scintillation measurements with DASS show that seeing was dominated by surface and boundary layers, except for the short periods (17:40 and 19h UT) when a layer at ≈ 3 km dominated the total seeing. However, note the striking anti-correlation of seeing and θ_0 !
GSM-wind: Two layers with winds blowing from the West at nearly the same speed. Another wind blowing from the South is measured at 17:42 UT and 17:54 UT.
Ground wind: NW until 19h, then SW. Sky: clear.

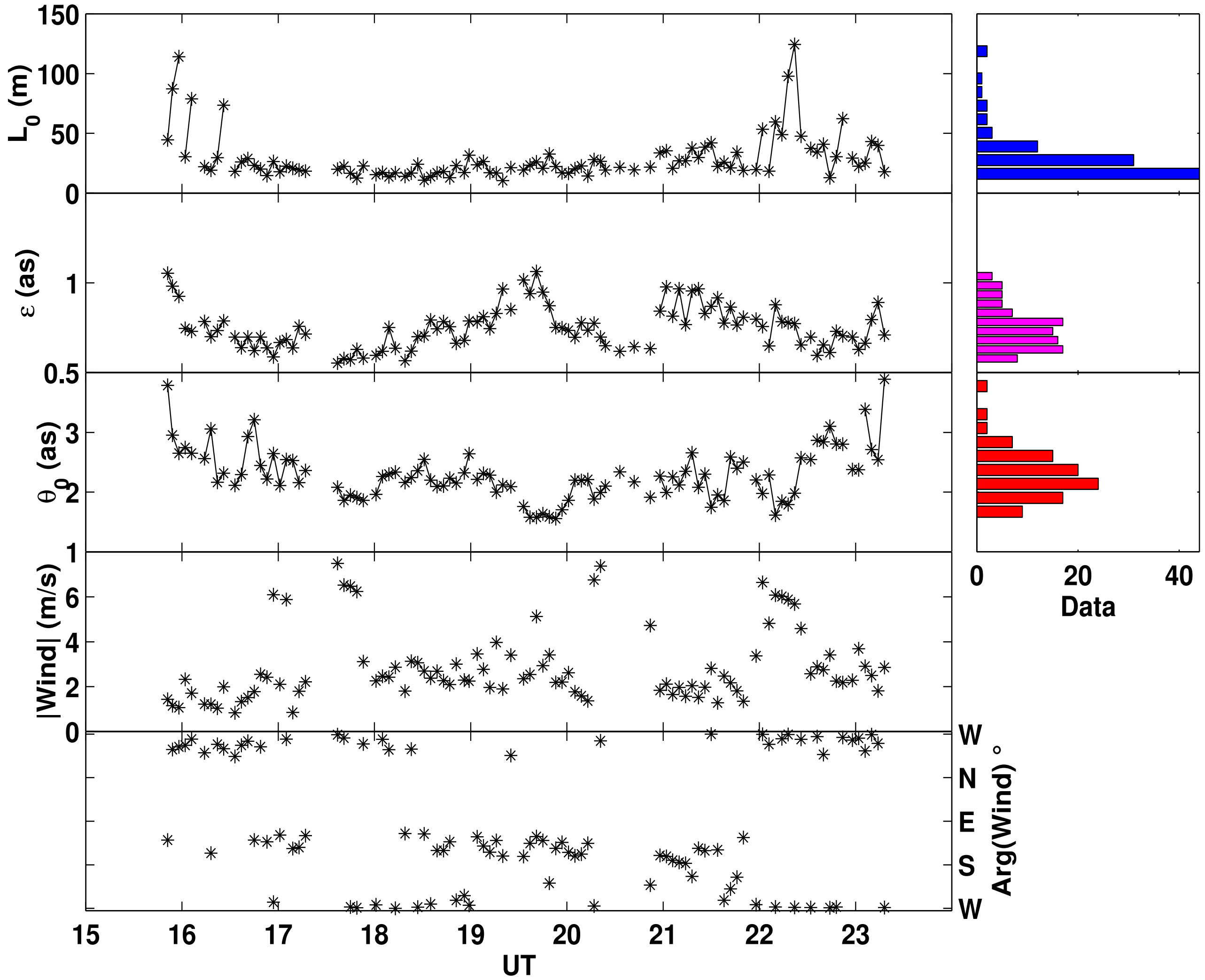

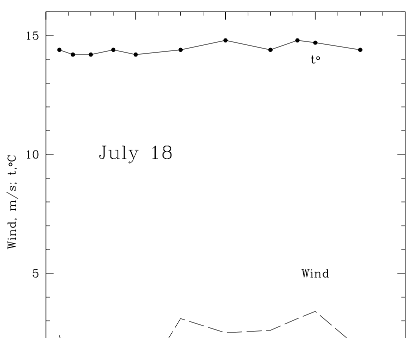

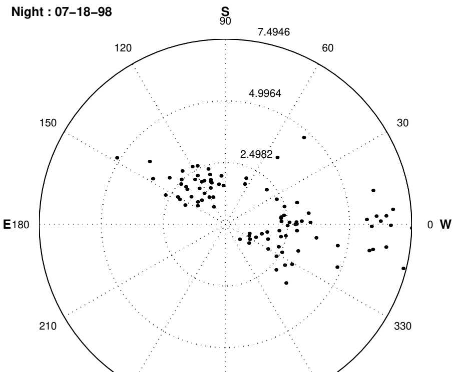

3. July 18/19

Seeing was slightly worse than average. Upper atmosphere above 1 km produced seeing of 0.4″, due to the turbulence in the tropopause ($h = 7 - 10$ km).
GSM-wind: Two layers with winds blowing from the West and the South–East.
Ground wind: N in the evening, E after 19h. Sky: clear.

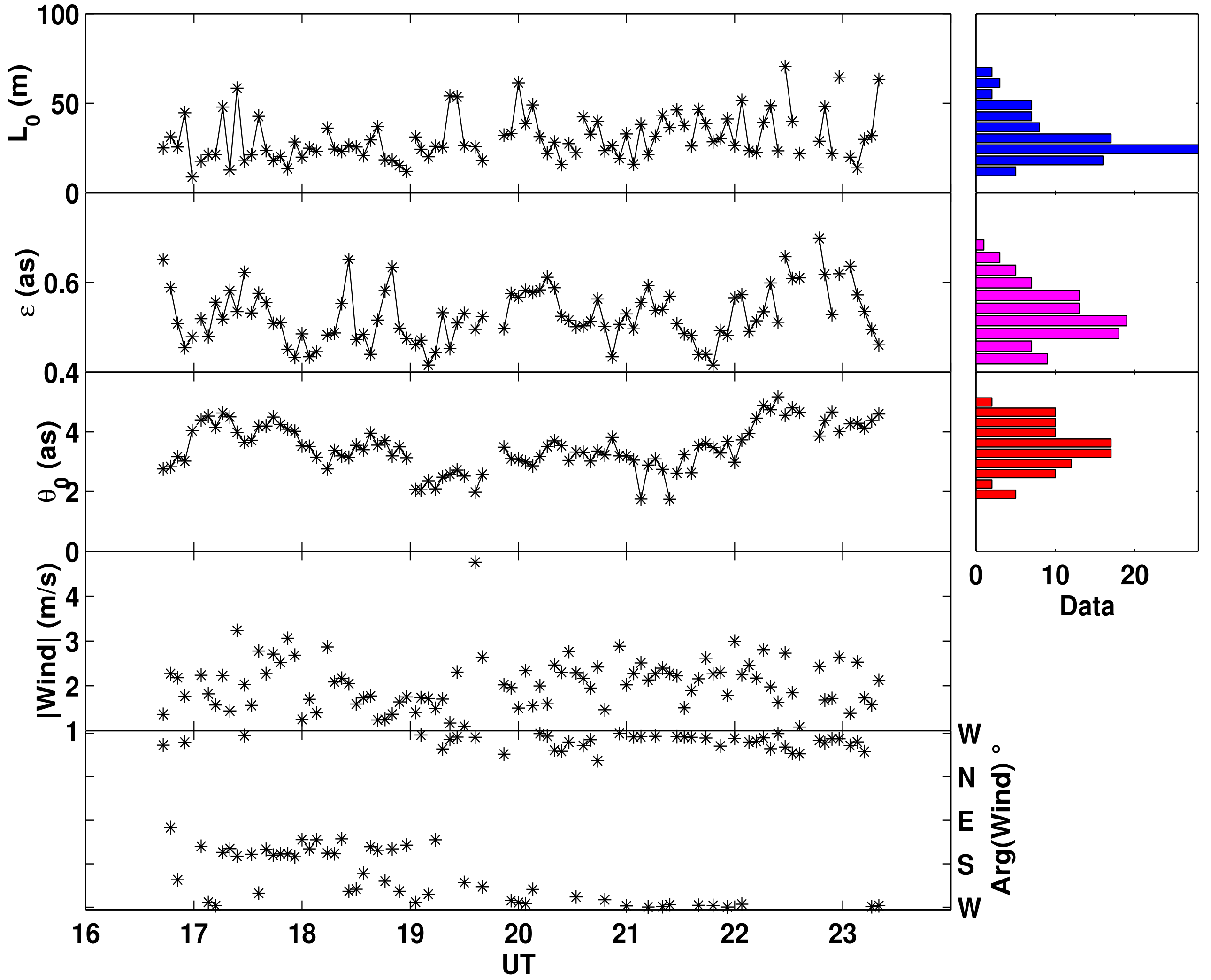

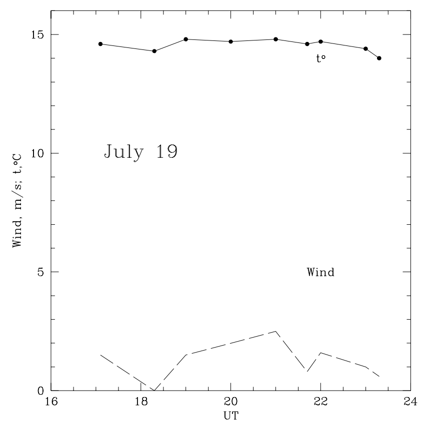

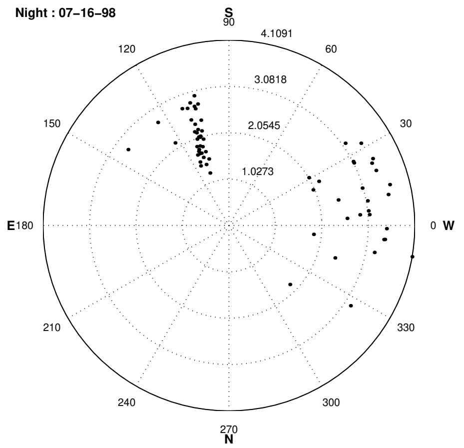

4. July 19/20

Night with the best, and very stable seeing. DASS data show that there was no turbulence at the tropopause, and upper-atmosphere seeing of $\approx 0.3''$ was generated by layers at an altitude of 4 km.

GSM-wind: Two layers with winds blowing from the West and the South–East at nearly the same speed. Another layer is seen on the cross–correlations but its associated peaks are never the highest. It blows approximately from the West.

Ground wind: E at 17h, then SW or W during the rest of the night. Sky: clear.

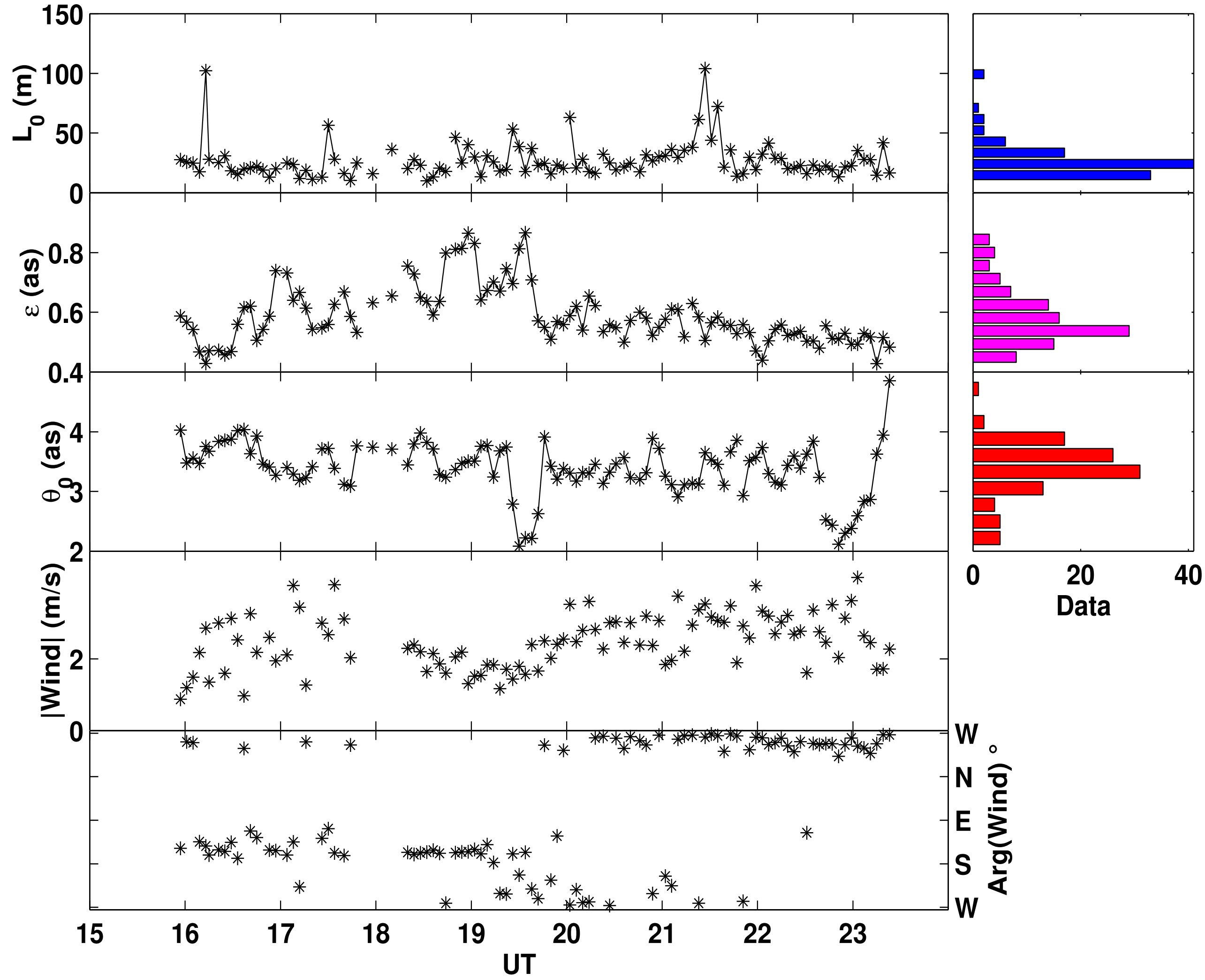

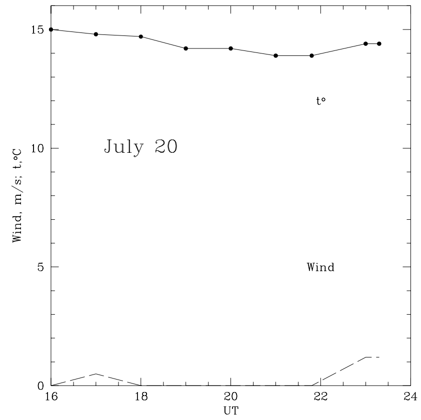

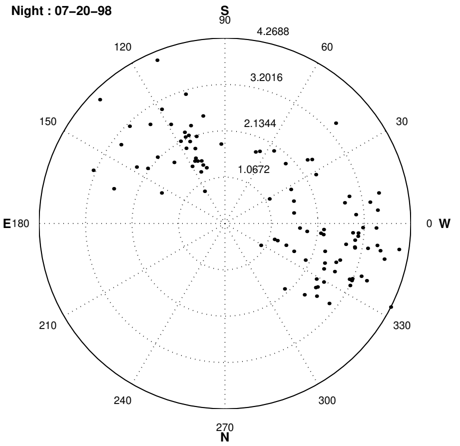

5. July 20/21

Seeing was better than average. From this night on the scintillation was measured with the SP1 photometer. Low scintillation and a large ratio of small/large aperture indices suggest that little turbulence was present at the tropopause, and scintillation originated mostly from layers at few km above mountain, like on previous night.
GSM-wind: Two layers with winds blowing from the West and the South–East at nearly the same speed. An another layer is seen on the cross–correlations but its associated peaks is never the highest. It blows approximately from the West.
Ground wind: NE in the evening, SE at dawn. Sky: clear.

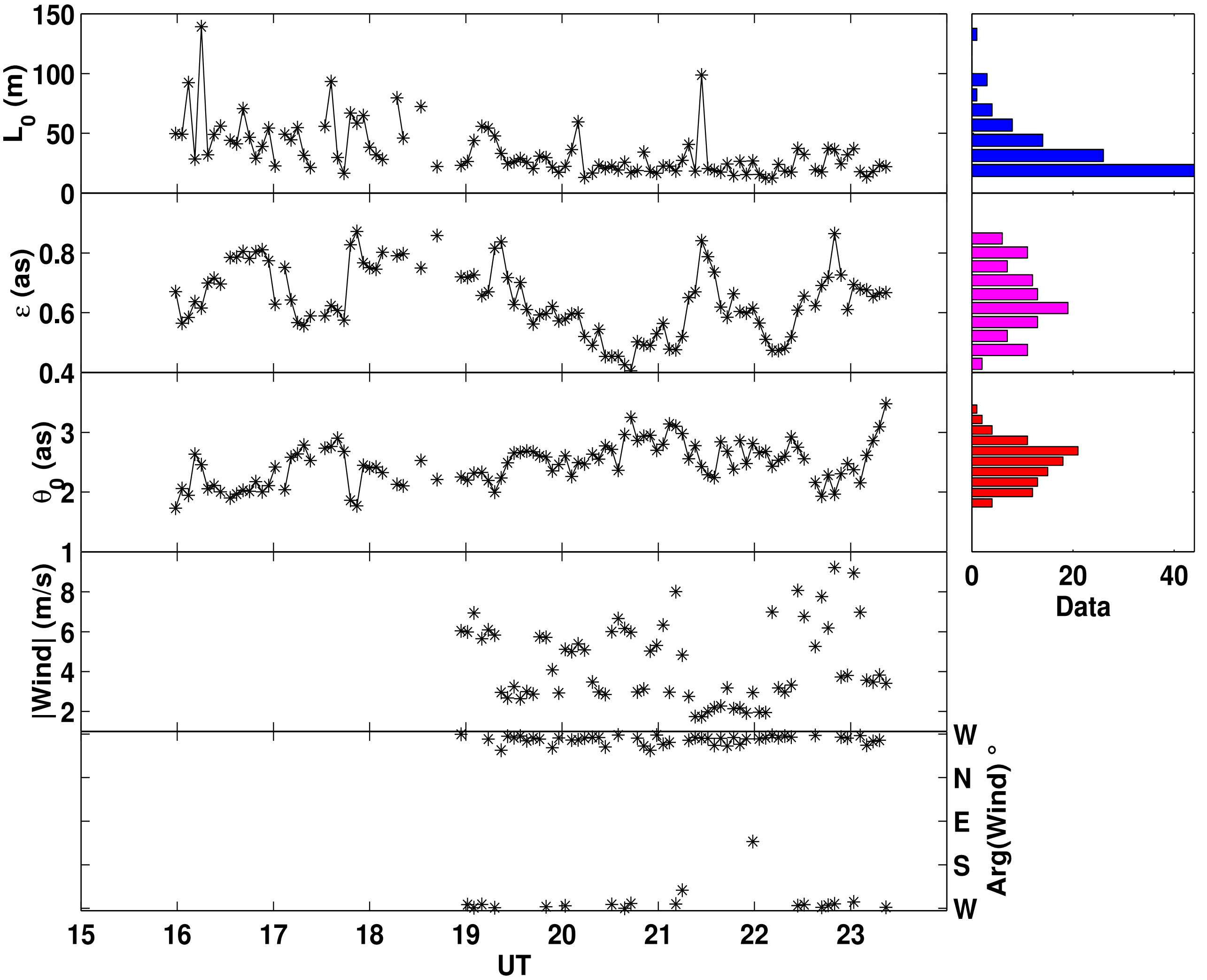

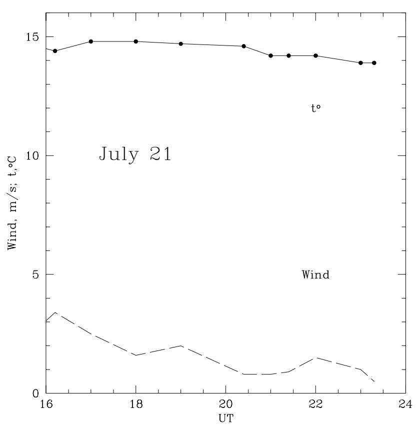

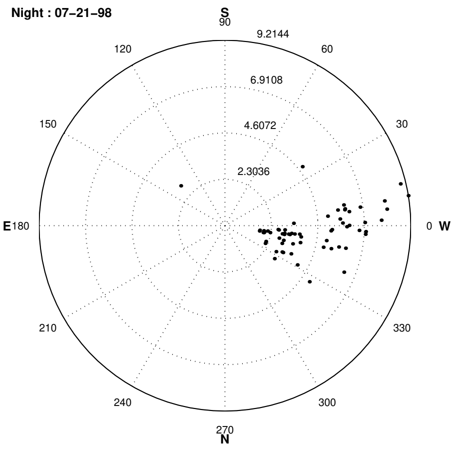

6. July 21/22

Some degradation of seeing and an increased scintillation can be noted, in comparison with the previous night. For the first 3 hours GSM worked in a linear configuration, wind data are not available for this period.

GSM-wind: Two layers with winds blowing from the West with two different speeds, and another one also from the West, but not measured.

Ground wind: NW in the evening, N after 19h. Sky: clear.

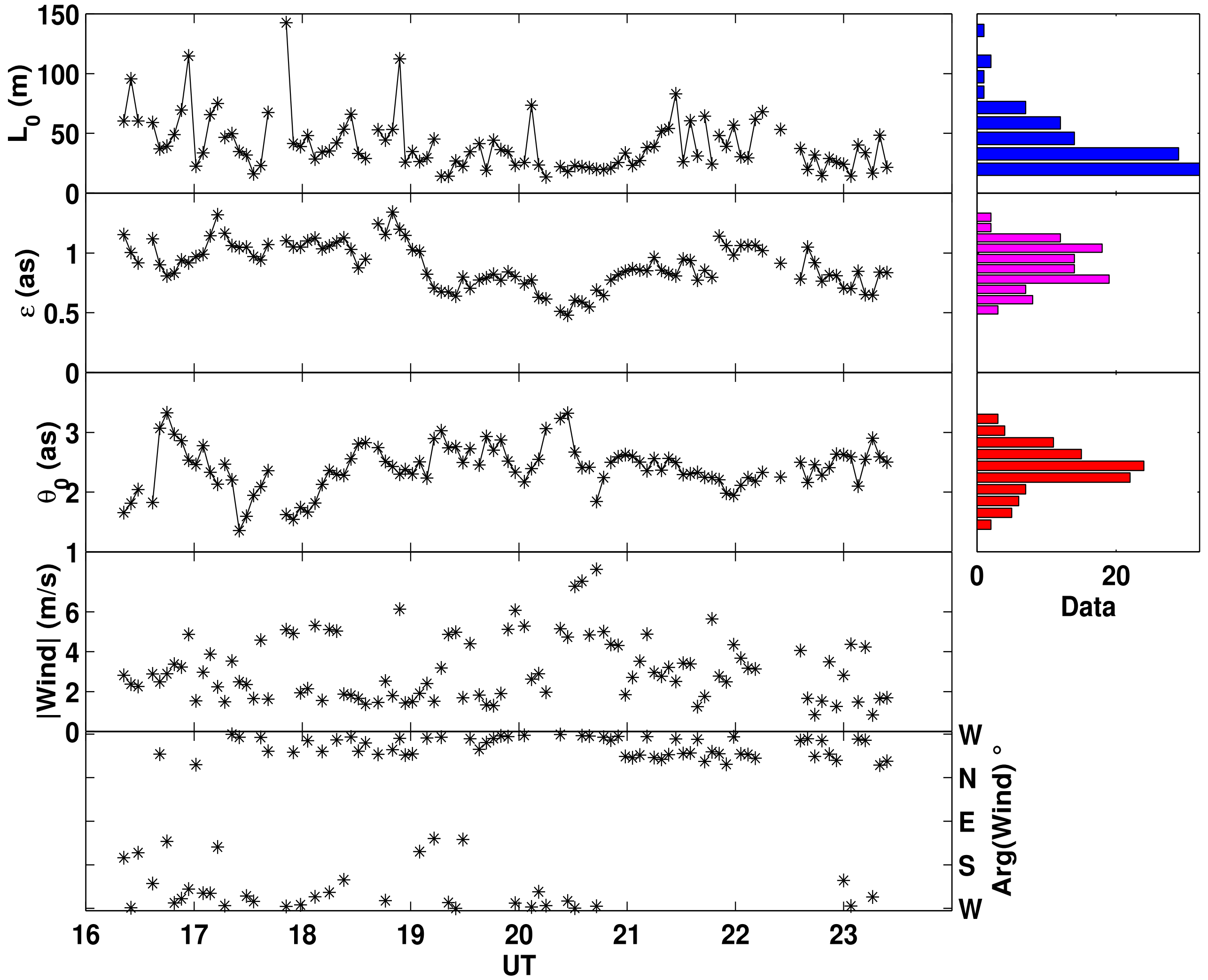

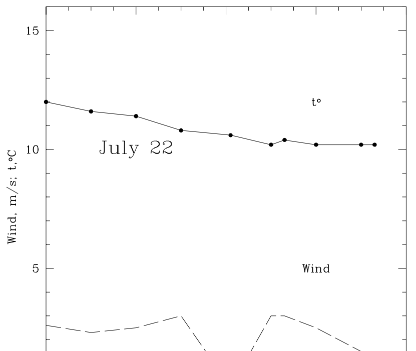

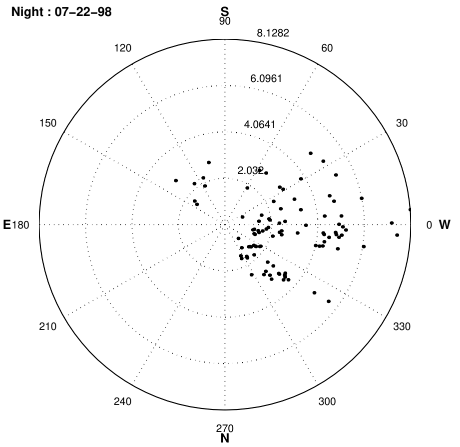

7. July 22/23

Seeing degrades with respect to the previous night. Note also the lower temperature.
GSM-wind: One layer with wind blowing from the South with intermittency and 3 layers with winds blowing from the West with different speeds.
Ground wind: NNW until 19h, turning to N by morning. Sky: clear.

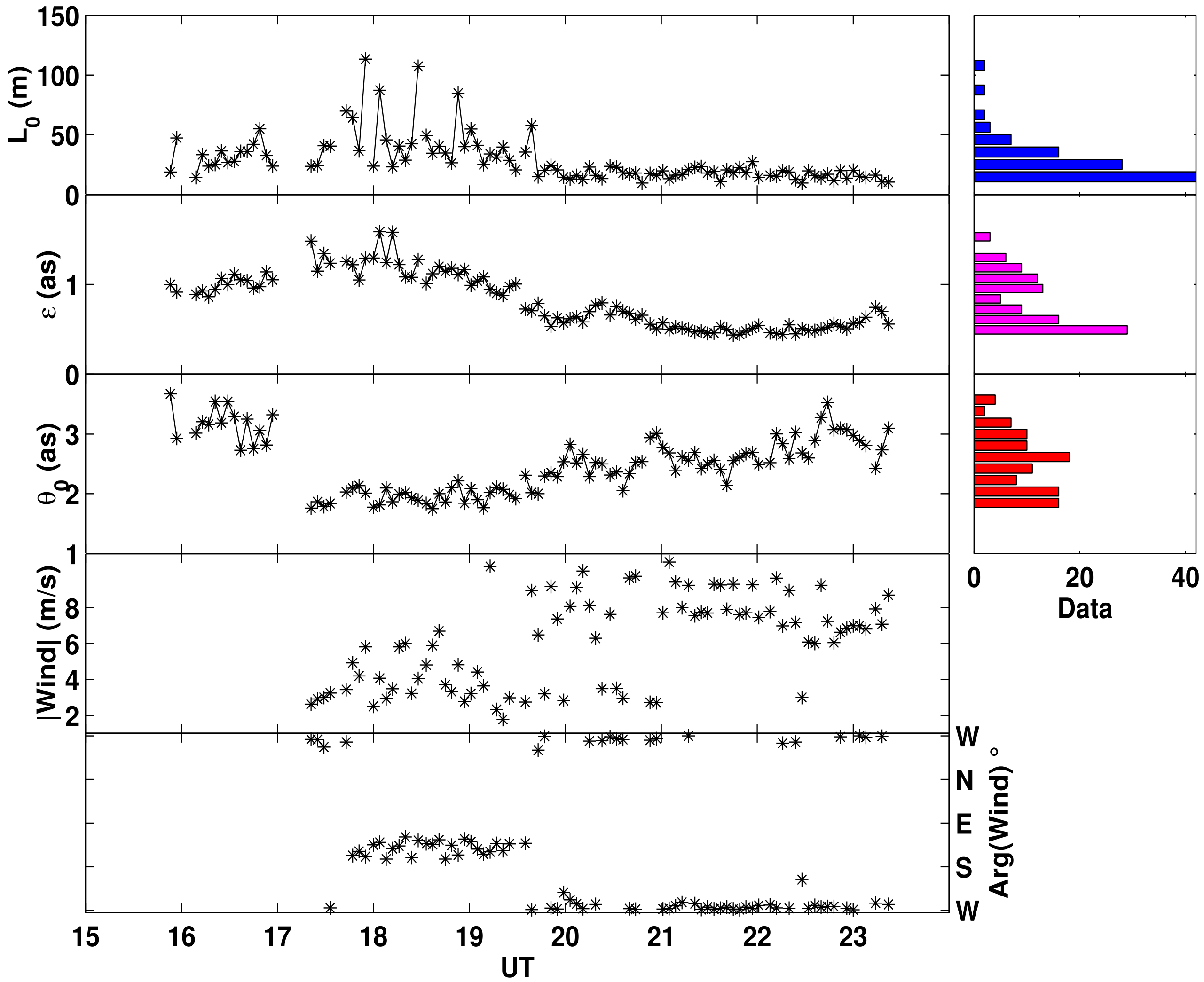

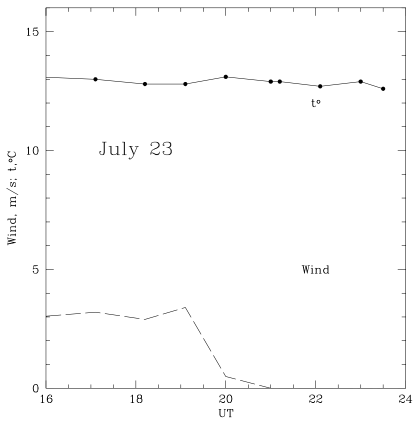

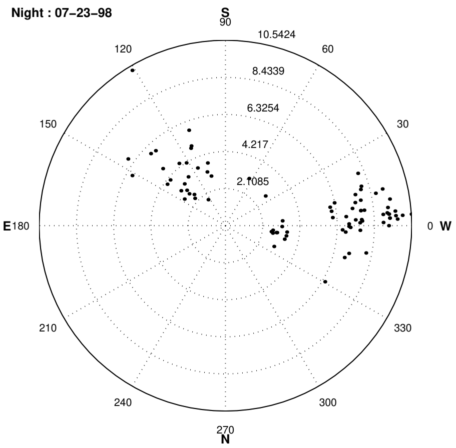

8. July 23/24

Little change with respect to the previous night. During the first hour, the two GSM modules were installed at the DIMM pier, 6.5 m above the ground, in order to verify that surface layer turbulence did not substantially contribute to the GSM seeing data.

GSM-wind: Two layers with winds blowing from the West and the South with nearly the same speed, or two other layers with winds blowing from the West with two different speeds.

Ground wind: between N and NE Sky: clear.

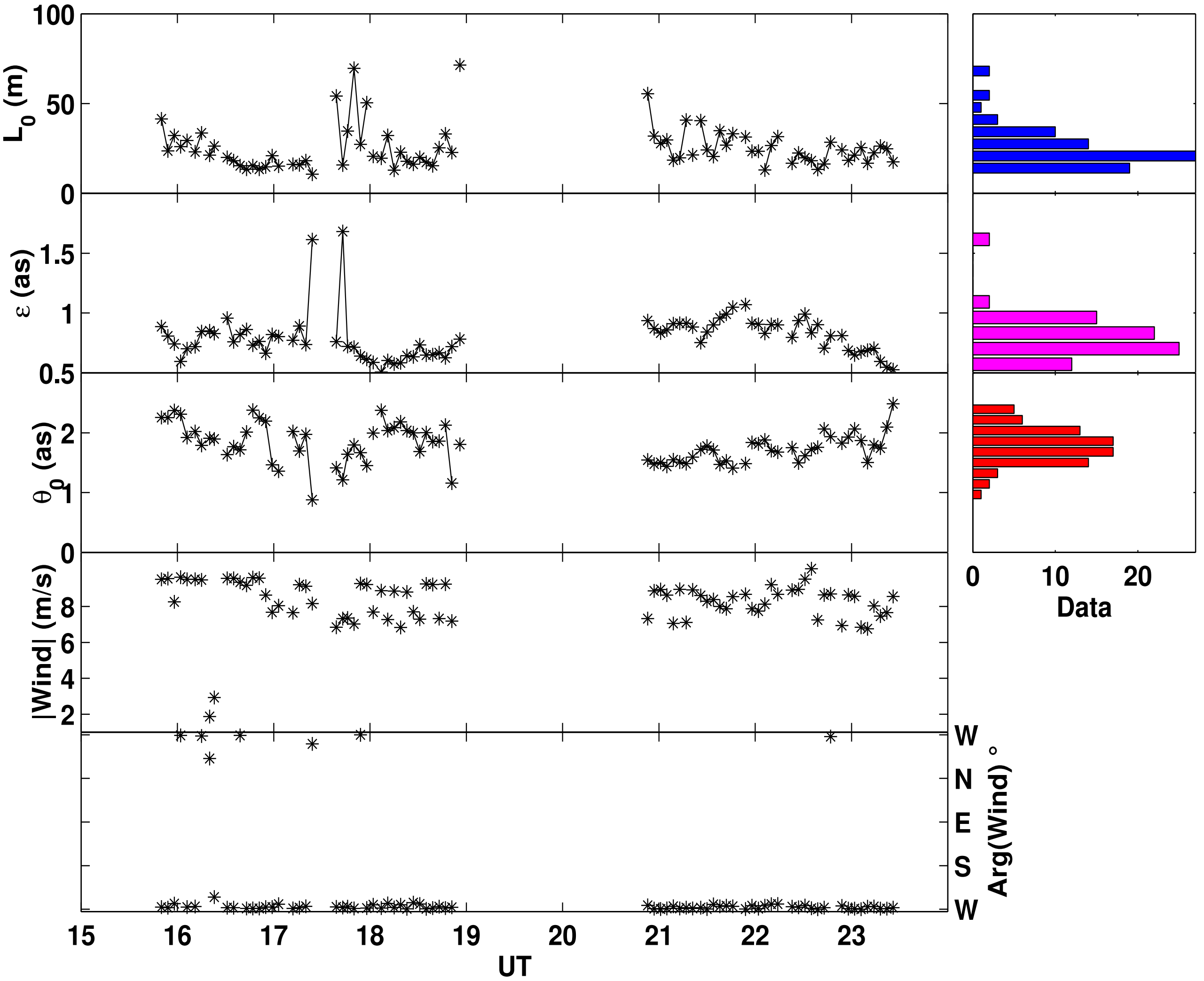

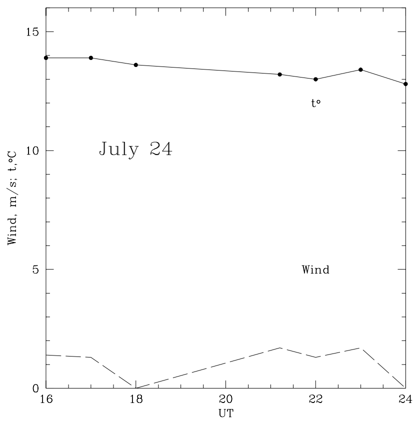

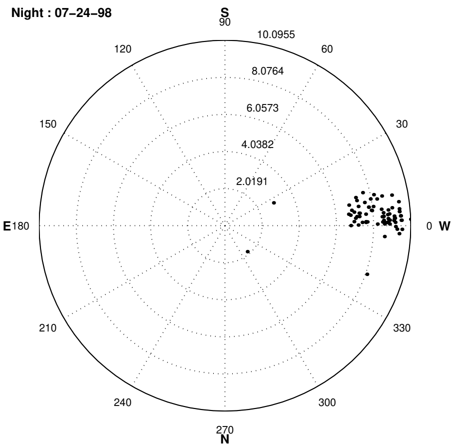

9. July 24/25

Last night of GSM operation. Measurements were interrupted from 19h to 21h UT due to clouds. Scintillation data indicate that turbulence at the tropopause gradually increased during these few nights, and reached its maximum on July 25/26.

GSM-wind: Two layers with winds blowing from the West with two different speeds.

Ground wind: N at 16h, SE at 17h, E after 19h. Sky: partially covered until 19h, cloudy till 21h, then clear.